Chemical Science

ROYAL SOCIETY OF CHEMISTRY

PERSPECTIVE

View Article Online
View Journal | View Issue

Cite this: *Chem. Sci.*, 2024, **15**, 19212

All publication charges for this article have been paid for by the Royal Society of Chemistry

Received 26th August 2024
Accepted 2nd November 2024

DOI: 10.1039/d4sc05707d

rsc.li/chemical-science

Cationic Al oxo-hydroxide clusters: syntheses, molecular structures, and functional applications

Naoki Ogiwara, Wei Zhou and Sayaka Uchida *

Al oxo-hydroxide clusters, synthesized through the hydrolysis of Al^{3+} solutions, are expected to bridge the gap between metal–aqua complexes and bulk metal oxides/hydroxides. These clusters exhibit remarkable diversity in structure and composition, controlled by modulating the basicity of the solution and use of capping ligands. While anionic metal–oxo clusters, such as polyoxometalates, have been extensively studied since the early 20th century, cationic metal–oxo clusters, including those of aluminum, have gained interest more recently due to their high reactivity and potential for various applications. We explore their molecular structures and assembly into various forms, including ionic crystals, amorphous solids, and hybrid materials, for applications such as adsorption, coagulation, and catalysis. Furthermore, we present future perspectives, emphasizing molecular design, scalable synthetic methods, and expanded functional applications, particularly in energy and environmental sciences, where these clusters are expected to demonstrate significant potential.

1. Introduction

Metal–oxo clusters are broadly defined as inorganic multi-metal molecular complexes with aqua (H_2O), hydroxide (OH^-), or oxide (O^{2-}) ligands.[1,2] These clusters can be considered intermediate compounds that bridge the gap between metal–aqua complexes and metal oxides/hydroxides. They are expected to exhibit intrinsic physicochemical properties not observed in either metal–aqua complexes or metal oxides/hydroxides. Anionic metal–oxo clusters known as polyoxometalates (POMs) comprise group V or VI metals (V, Nb, Ta, Mo, W) and oxide ligands. POMs encompass extensive research areas, with their significance dating back to 1933 when Keggin reported the structure of $[PW_{12}O_{40}]^{3-}$ through X-ray diffraction analysis.[3–8] On the other hand, main group metals (Al, Sb, Bi, *etc.*),[9–14] group IV metals (Ti, Zr, Hf),[15,16] or other metals (Fe, U, Np, *etc.*)[17,18] with lower oxidation states and electronegativity form cationic metal–oxo clusters. These clusters often possess labile hydroxide and aqua ligands on their molecular surfaces, making crystallization more difficult. Consequently, due to their high reactivity, cationic metal–oxo clusters represent an emerging research field for functional applications.

Among the cationic metal–oxo clusters, aluminum (Al) oxo-hydroxide clusters have long been a subject of significant interest.[9] Al, comprising about 8% by weight of the Earth's crust, is a typical metal prevalent in a wide variety of minerals.[19,20] Aluminum oxides and hydroxides are widely used in applications such as adsorbents, heterogeneous catalysis, and coagulation processes.[21–23] However, the compositions and structures of oxides (*e.g.*, α, γ-type) and hydroxides (*e.g.*, gibbsite, boehmite) are limited. Therefore, the use of clusters as components is expected to extend the compositions, structures, and functionalities of unexplored solid-state materials. Al species are present not only in the solid state but also in natural water systems, where Al^{3+} aqua ions hydrolyze, giving rise to a diverse array of Al oxo-hydroxide clusters. These clusters influence geochemical processes and soil chemistry, affecting Al floc formation in polluted streams and impacting bioavailability and phytotoxicity in ecosystems.[24–26] They also hold potential for practical applications, including use as antiperspirants,[27] anionic coagulants in water treatment,[28] and precursors for fabricating thin film devices from aqueous solutions.[29] In 2006, Casey reported a seminal review on cutting-edge research of Al oxo-hydroxide clusters at that time.[9] Since the review's publication, the structural diversity of these clusters has increased, and molecular design strategies have been proposed, leading to the synthesis of metal-substituted Al oxo-hydroxide clusters and new applications, particularly in the solid state.

In this perspective, we aim to present the synthetic strategies for Al oxo-hydroxide-based clusters, focusing on designing their compositions and molecular structures. The assembly of these clusters for functional applications, such as adsorptive removal of pollutants and catalysis, will also be discussed.

2. Syntheses and molecular structures of Al oxo-hydroxide clusters

2.1 Al oxo-hydroxide clusters

Among Al oxo-hydroxide clusters, the Keggin-type $[Al_{13}O_4(OH)_{24}(H_2O)_{12}]^{7+}$ ($\mathbf{Al_{13}}$) structure is widely recognized as the most

Department of Basic Science, School of Arts and Sciences, The University of Tokyo, Komaba, Meguro-ku, Tokyo, 153-8902, Japan. E-mail: csayaka@g.ecc.u-tokyo.ac.jp

well-known. In the Keggin-type **Al_{13}**, a central tetrahedral [AlO_4] unit is surrounded by four $Al_3(OH)_6(H_2O)_3$ trimers, and three rotational isomers (ε, δ, γ) of the Keggin-type **Al_{13}** has been successfully isolated. In 1960, Johansson and coworkers reported ε-Keggin-type **Al_{13}** (**ε-Al_{13}**) with T_d molecular symmetry (Fig. 1a),[30,31] in which the four surrounding $Al_3(OH)_6(H_2O)_3$ trimers are connected through edge-sharing of hydroxyl groups. **ε-Al_{13}** was synthesized by thermal hydrolysis of an aqueous Al^{3+} solution, and in 1991, Nazar and coworkers found that thermal aging of **ε-Al_{13}** in the presence of Na^+ ions produced a new polycation, later identified as δ-Keggin-type **Al_{13}** (**δ-Al_{13}**, Fig. 1b).[32] In **δ-Al_{13}**, one of the four $Al_3(OH)_6(H_2O)_3$ trimers is rotated 60° relative to the remaining structure of **ε-Al_{13}**.[33] **δ-Al_{13}** possesses C_{3v} molecular symmetry, and the average bond distance of tetrahedral [AlO_4] unit of **δ-Al_{13}** is 1.80 Å, which is shorter than that of **ε-Al_{13}** (1.83 Å). In 2013, Pan and coworkers reported γ-Keggin-type **Al_{13}** (**γ-Al_{13}**, Fig. 1c), in which two of the four $Al_3(OH)_6(H_2O)_3$ trimers are rotated 60° relative to the remaining structure of **ε-Al_{13}**.[34] The formation of **γ-Al_{13}** was achieved through the thermal hydrolysis of an Al^{3+}-containing solution in the presence of $Ca(OH)_2$ and glycine. ^{1}H diffusion-ordered spectroscopy (DOSY) and ^{27}Al NMR data indicate that glycine binds to the **Al_{13}** isomers, suggesting that this binding is a crucial step in the isomerization process.[35] The authors propose that glycine serves as a buffer during the initial addition of base, preventing nonspecific hydrolysis by weakly and reversibly binding to Al^{3+} species. They also suggest that Ca^{2+} ions are essential in enabling the stepwise rotation of the trimeric subunits during this process. The molecular symmetry of **γ-Al_{13}** is categorized as C_{2v}, and the average bond distance of the tetrahedral [AlO_4] unit of **γ-Al_{13}** (1.78 Å) is shorter than that of **ε-Al_{13}** (1.83 Å) and **δ-Al_{13}** (1.80 Å). In 2016, Cheong, Pan, Casey, and coworkers observed a peak at 72 ppm in the ^{27}Al NMR spectra of thermally aged **ε-Al_{13}** solution in the presence of glycine and $CaCl_2$, which differed from the peak positions of tetrahedral Al in **ε-Al_{13}** or **δ-Al_{13}**, indicating the presence of a different rotational isomer,[35] while the attempts for isolation were unsuccessful.

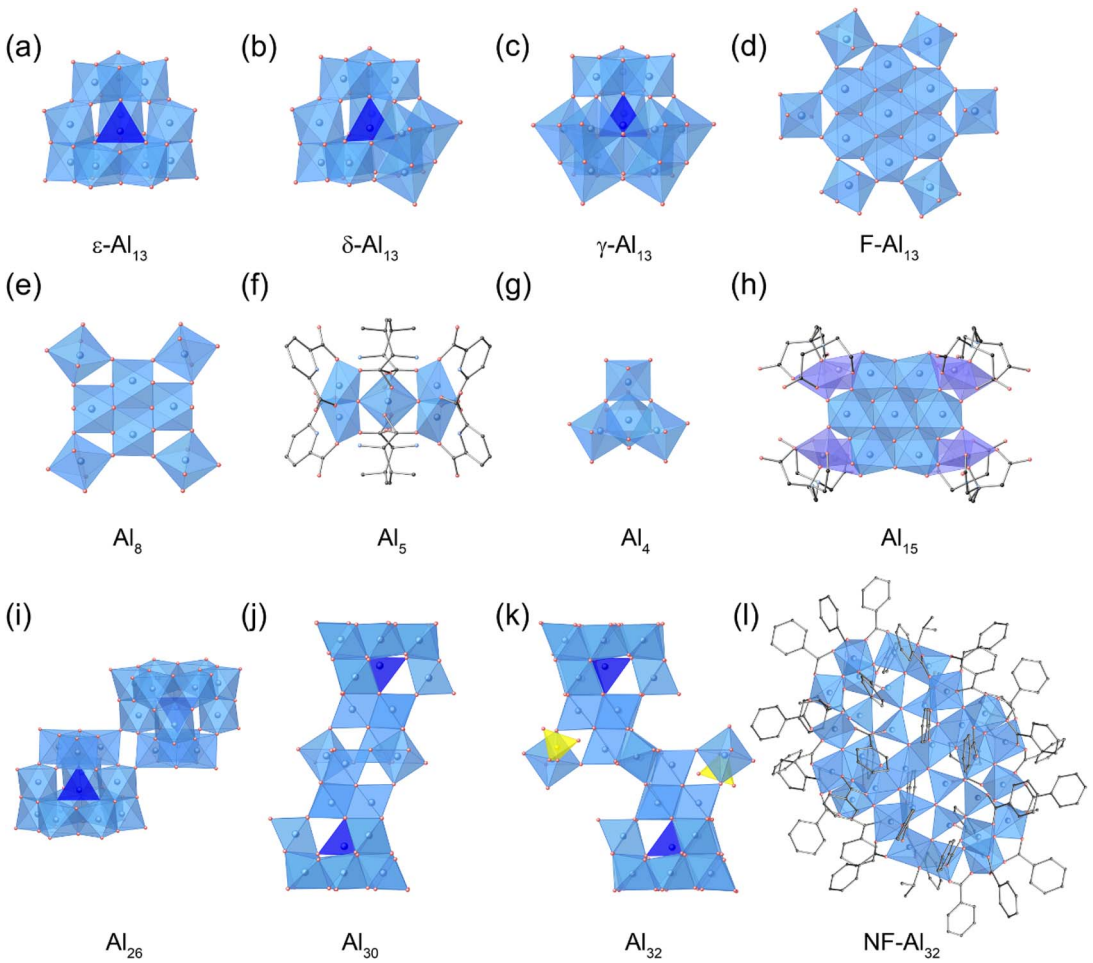

Fig. 1 Molecular structure of (a) [ε-$Al_{13}O_4(OH)_{24}(H_2O)_{12}]^{7+}$ (**ε-Al_{13}**), (b) [δ-$Al_{13}O_4(OH)_{24}(H_2O)_{12}]^{7+}$ (**δ-Al_{13}**), (c) [γ-$Al_{13}O_4(OH)_{24}(H_2O)_{12}]^{7+}$ (**γ-Al_{13}**), (d) $[Al_{13}(OH)_{24}(H_2O)_{24}]^{15+}$ (**F-Al_{13}**), (e) $[Al_8(OH)_{14}(H_2O)_{18}]^{10+}$ (**Al_8**), (f) $[Al_5O_2(OH)_2(HPDA)_4(_L\text{-Val})_4]^+$ (**Al_5**), (g) $[Al_4(OH)_6(H_2O)_{12}]^{6+}$ (**Al_4**), (h) $[Al_{15}O_4(OH)_{20}(hpdta)_4]^{3-}$ (**Al_{15}**), (i) $[Al_{26}O_8(OH)_{50}(H_2O)_{20})]^{12+}$ (**Al_{26}**), (j) $[Al_{30}O_8(OH)_{56}(H_2O)_{26}]^{18+}$ (**Al_{30}**), and (k) $[Al_{32}O_8(OH)_{60}(H_2O)_{28}(SO_4)_2]^{16+}$ (**Al_{32}**), (l) $[Al_{32}(benzoate)_{36}(O^iPr)_4(\mu_3\text{-}O)_{24}(\mu_4\text{-}O)_4]$ (**NF-Al_{32}**). [AlO_6], [AlO_4] and [SO_4] are shown by the light blue, dark blue, and yellow polyhedrons, respectively.

In 1995, Heath and coworkers carried out the thermal hydrolysis of an aqueous Al^{3+} solution with *N*-(2-hydroxyethyl) iminodiacetic acid (H_3heidi = $HOCH_2CH_2N(CH_2COOH)_2$) and discovered the formation of a flat-shaped **Al_{13}** cluster composed entirely of octahedral [AlO_6] units ([$Al_{13}(\mu_3\text{-}OH)_6(\mu_2\text{-}OH)_{12}$(heidi)$_6(H_2O)_6]^{3+}$, **F-$Al_{13}$**·heidi).[36] In **F-$Al_{13}$**·heidi, an [$AlO_6$] core is surrounded by six additional [AlO_6] units connected *via* μ_3-OH bridges, creating a coplanar configuration. Six more [AlO_6] octahedra are alternately attached above and below the primary plane through shared oxygen vertices. In 1998, Seichter and coworkers crystallized the all-inorganic $[Al_{13}(OH)_{24}(H_2O)_{24}]^{15+}$ (**F-Al_{13}**, Fig. 1d) as chloride salts through a slow hydrolysis of an aqueous Al^{3+} solution at ambient conditions.[37] In 2008, Johnson and coworkers modified the synthetic method for **F-Al_{13}** by hydrolyzing an Al^{3+} solution with nitrosobenzene in MeOH, resulting in a high yield.[38] However, the high toxicity of nitroso-containing compounds hindered the large-scale synthesis of **F-Al_{13}**. To overcome this drawback, in 2011, Keszler and coworkers used Zn metal as a base to hydrolyze Al species, enabling the large-scale preparation of **F-Al_{13}**.[39] Conventional base titration produces a locally high pH environment, facilitating the nucleation of tetrahedral $[Al(OH)_4]^-$ species, which condense with six-coordinate Al^{3+} aqua ions to form a Keggin structure. In contrast, the dissolution of Zn metal gradually increases the pH, offering a direct route to form the **F-Al_{13}** clusters with a good yield. In 2013, Cheong, Fang, Keszler, and coworkers electrolytically synthesized **F-Al_{13}**.[40] To increase the pH of Al^{3+}-containing solution and produce **F-Al_{13}**, they utilized the reduction of protons to hydrogen gas in the cathode compartment of a two-compartment electrochemical cell, instead of using a base. They also proposed that **F-Al_{13}** forms *via* an intermediate, $[Al_7(OH)_{12}(H_2O)_{12}]^{9+}$, which represents the planar core of **F-Al_{13}**, as indicated by Raman spectroscopy and computational studies. The synthesis of **F-Al_{13}** can be achieved through both bottom-up and top-down methods. In 2017, Keszler, Hutchison, Johnson, and coworkers synthesized **F-Al_{13}** by direct dissolution of aluminum hydroxide in nitric acid.[41] They also demonstrated that **F-Al_{13}** is applicable as a precursor to prepare near-atomically smooth Al_2O_3 thin films.[29]

The diversity in cluster size and shape is a notable feature of Al oxo-hydroxide clusters. Cluster downsizing was achieved by inhibiting growth through a decrease in basicity and the use of capping ligands during the hydrolysis of an Al^{3+} solution. In 2005, Casey and coworkers conducted a long-term (7 years) hydrolysis of an acidic Al^{3+} solution, resulting in the discovery of a smaller Al oxo-hydroxide octamer, $[Al_8(OH)_{14}(H_2O)_{18}]^{10+}$ (**Al_8**, Fig. 1e).[42] The **Al_8** cluster exhibits a flat-shaped structure, with the central four [AlO_6] units connected by edge-sharing, while the peripheral four [AlO_6] units are linked through corner-sharing. In 2016, Limberg and coworkers trapped **Al_8** during the hydrolysis of Al species with the aid of capping ligands (*p*-anisylSi$(OSiPh_2OH)_3$), yielding a trisilanol-capped octameric cluster, $[Al_8(\mu_3\text{-}OH)_2(\mu_2\text{-}OH)_{10}(THF)_3$(*p*-anisylSi$(OSiPh_2O)_3)_4]$.[43] In 2017, Johnson, Keszler, and coworkers demonstrated a facile synthesis of capping-free **Al_8** through the hydrolysis of Al species in a sulfate-rich aqueous solution.[44] In 2024, Fang and co-workers conducted the hydrolysis of a *n*-propanolic Al^{3+} solution with L-valine (L-Val) and pyridine-2,6-dicarboxylic acid (H_2PDA), resulting in the formation of $[Al_5O_2(OH)_2(HPDA)_4$(L-Val)$_4]^+$ (**Al_5**, Fig. 1f), which features vertex-sharing of two triangles $[Al_3O(OH)(HPDA)_2]^{4+}$.[45] In 2011, Sun and co-workers crystallized a vertex-shared tetrahedral $[Al_4(OH)_6(H_2O)_{12}]^{6+}$ (**Al_4**, Fig. 1g) with $[Al(OH_2)_6]^{3+}$ and Br^- as $[Al_4(OH)_6(H_2O)_{12}][Al(H_2O)_6]_2Br_{12}$ (**Al_4**·Al_2Br_{12}) in a cubic $Fd\bar{3}m$ space group.[46] The tetrahedral **Al_4** with T_d symmetry is constructed by the linkage of four distorted [AlO_6] octahedra through vertex-sharing of hydroxyl groups.

Al oxo-hydroxide clusters larger than **Al_{13}** have been explored by promoting cluster growth through the hydrolysis of an Al^{3+} solution under relatively harsh conditions—specifically by increasing the basicity of the reaction solution, aging temperature, and reaction times. In 2001, Powell and coworkers performed the hydrolysis of an Al^{3+} solution with a base (piperazine) and hpdta ligand (H_5hpdta = $HOCH_2[CH_2N(CH_2COOH)_2]_2$), resulting in the formation of $[Al_{15}O_4(OH)_{20}(hpdta)_4]^{3-}$ (**Al_{15}**, Fig. 1h).[47] **Al_{15}** possesses an inner $\{Al_7(OH)_{12}\}^{9+}$ core, similar to **F-Al_{13}**, which is encapsulated by four dinuclear {Al_2(hpdta)} units to form **Al_{15}**. In 2012, Forbes and coworkers refluxed an Al^{3+} aqueous solution in the presence of 2,6-napthalene disulfonate (2,6-NDS) to obtain $[Al_{26}O_8(OH)_{50}(H_2O)_{20})]^{12+}$ (**Al_{26}**, Fig. 1i).[48] In **Al_{26}**, two **δ-Al_{13}** clusters are linked *via* vertex-sharing through rotated $[Al_3(\mu_2\text{-}OH)_6(H_2O)_3]$ trimer groups. In 2000, $[Al_{30}O_8(OH)_{56}(H_2O)_{26}]^{18+}$ (**Al_{30}**, Fig. 1j) was synthesized through the thermal hydrolysis of a basic Al^{3+} aqueous solution.[33,49] Al NMR studies suggest that **Al_{30}** forms when thermal treatment of **ε-Al_{13}** produces [AlO_6] units, which then attach to undissociated **ε-Al_{13}**, promoting isomerization to **δ-Al_{13}**. Two unstable **δ-Al_{13}** monomers stabilize by dimerization with four [AlO_6] units, resulting in the dimeric **Al_{30}** structure. In 2010, Bi and coworkers carried out density functional theory (DFT) study and kinetic analysis to address the formation mechanism of **Al_{30}**.[50] They proposed a three-step process: (1) isomerization from **ε-Al_{13}** to **δ-Al_{13}**; (2) stabilization of **δ-Al_{13}** by Na^+ to form Na-**δ-Al_{13}**, followed by replacement of Na^+ with Al monomers in solution to produce **δ-Al_{14}**; and (3) reaction of two **δ-Al_{14}** with two Al monomers, leading to the formation of **Al_{30}**. In 2012, Forbes and coworkers reported that **Al_{30}** can be crystallized with 2,6-NDS as $(Al_2O_8Al_{28}(OH)_{56}(H_2O)_{26})$(2,6-NDS)$_8$-$Cl_2(H_2O)_{34}$.[48] In 2011, Sun and coworkers conducted the hydrolysis of an Al^{3+} aqueous solution under hydrothermal conditions to obtain $[Al_{32}O_8(OH)_{60}(H_2O)_{28}(SO_4)_2]^{16+}$ (**Al_{32}**, Fig. 1k).[51] **Al_{32}** possesses a structure similar to that of **Al_{30}**, but with four μ_1-H_2O molecules, which exhibit strong acidity in **Al_{30}**, replaced by two $[Al(OH)_2(H_2O)_3(SO_4)]^-$ groups. In 2021, Fang, Zhang, and coworkers synthesized **Al_{32}** with a hydrotalcite-like nanoflake structure, $[Al_{32}$(benzoate)$_{36}(O^iPr)_4(\mu_3\text{-}O)_{24}(\mu_4\text{-}O)_4]$ (**NF-Al_{32}**, Fig. 1l), by controlling the hydrolysis of Al^{3+} ions in the presence of π-conjugated carboxylate ligands.[52]

The size control of ring-shaped Al oxo-hydroxide clusters as well as spherical and elliptical clusters has been achieved. In 2020, Fang, Zhang, and coworkers synthesized ring architectures of Al oxo-hydroxide clusters with general formula $[Al(OH)_x(OR)_y(R'OOCPh)_{3-x-y}]$ ($x = 0, y = 2$; $x = 0.5, y = 1$; R = Me, Et, ^{n}Pr, ^{n}But; R′ = H, F, Cl, NH_2, NO_2, CH_3) by solvothermal

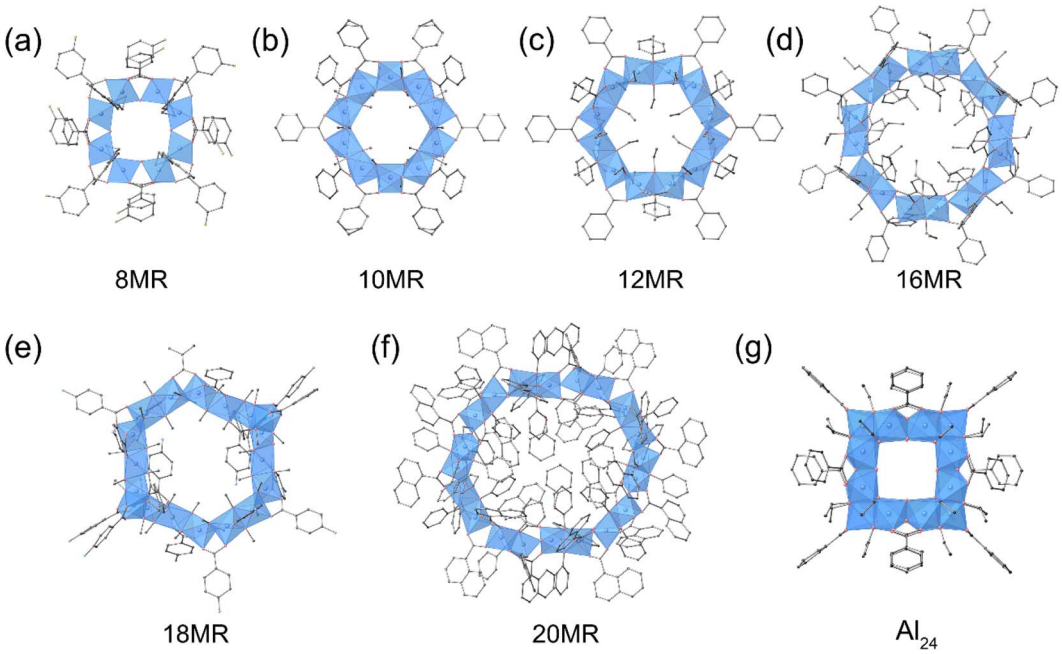

Fig. 2 Molecular structure of (a) $[Al_8(OH)_4(3\text{-fluorobenzoate})_{12}(OBut^n)_8]$ (**8MR**), (b) $[Al_{10}(benzoate)_{10}(OMe)_{20}]$ (**10MR**), (c) $[Al_{12}(benzoate)_{12}(OEt)_{24}]$ (**12MR**), (d) $([Al_{16}(OH)_8(benzoate)_{24}(OPr^n)_{16}]$ (**16MR**), (e) $[Al_{18}(4\text{-aminobenzoate})_{18}(OMe)_{36}]$ (**18MR**), (f) $[Al_{20}(phenol)_{20}(OH)_{10}(1\text{-naphthalenecarboxylate})_{30}]$ (**20MR**), and (g) $[Al_{24}(BA)_{12}(EtO)_{24}(OH)_{32}]^{4+}$ (**Al_{24}**).

method.[53] The proper choice of the type of monohydric alcohols and benzoate derivatives could systematically tune the ring size of clusters from 8-membered ring (**8MR**, $[Al_8(OH)_4(3\text{-fluorobenzoate})_{12}(OBut^n)_8]$, Fig. 2a) to **10MR** $[Al_{10}(benzoate)_{10}(OMe)_{20}]$, Fig. 2b), **12MR** ($[Al_{12}(benzoate)_{12}(OEt)_{24}]$, Fig. 2c), and **16MR** ($[Al_{16}(OH)_8(benzoate)_{24}(OPr^n)_{16}]$, Fig. 2d). In 2022, the same group expanded the ring size to **18MR** ($[Al_{18}(4\text{-aminobenzoate})_{18}(OMe)_{36}]$ Fig. 2e) by introducing hydrophilic amide functional groups,[54] and **20MR** ($[Al_{20}(phenol)_{20}(OH)_{10}(1\text{-naphthalenecarboxylate})_{30}]$, Fig. 2f) through phenol-thermal synthesis.[55] In 2022, the same group constructed an Al oxo-hydroxide cluster with a cage structure, $[Al_{24}(benzoate)_{12}(OEt)_{24}(OH)_{32}]^{4+}$ (**Al_{24}**, Fig. 2g), by refluxing an Al^{3+} ethanolic solution with benzoate ligands.[56] The **Al_{24}** cage features a truncated hexahedron topology and is composed of six octagonal Al_8 faces and eight triangular Al_3 faces, forming an internal cavity with a volume of approximately 320 Å^3.

2.2 Metal substituted Al oxo-hydroxide clusters

Since alumina-based solid solutions (*e.g.*, Cr^{3+}-doped alumina, ruby) and mixed oxides (*e.g.*, $MgAl_2O_4$, spinel) exhibit interesting functionalities distinct from those of pure oxides,[57,58] incorporating other metals into Al oxo-hydroxide clusters would also be a promising approach to explore the compositional and structural diversity, and potential applications. An early work involves the substitution of Ge^{4+} ions for the central tetrahedral $[AlO_4]$ in **ε-Al_{13}**, forming $[\varepsilon\text{-}GeO_4Al_{12}(OH)_{24}(H_2O)_{12}]^{8+}$ (**ε-$GeAl_{12}$**, Fig. 3a). **ε-$GeAl_{12}$** was synthesized by Görz, Schönherr, and coworkers in 1983 through the hydrolysis of a mixed aqueous solution containing Al^{3+} and Ge^{4+} ions.[59] In 2001, Casey and coworkers investigated the molecular structure of **ε-$GeAl_{12}$** using single-crystal X-ray diffraction and solid-state ^{27}Al MAS NMR spectroscopy.[60] Their investigations revealed that **ε-$GeAl_{12}$** exhibits an overall point group symmetry of D_{2h}, whereas **ε-Al_{13}** shows T_d symmetry. The substitution of Ge^{4+} in the central position induces a tetragonal distortion in **ε-$GeAl_{12}$**, characterized by a slight expansion in both axial and equatorial directions. Görz, Schönherr, and coworkers synthesized a Ga-substituted Al cluster with T_d symmetry, $[\varepsilon\text{-}GaO_4Al_{12}(OH)_{24}(H_2O)_{12}]^{7+}$ (**ε-$GaAl_{12}$**, Fig. 3b) through the hydrolysis of a mixed aqueous solution containing Al^{3+} and Ga^{3+} ions.[61,62] Kydd and coworkers characterized **ε-$GaAl_{12}$** by MAS NMR, IR, and PXRD, highlighting that the central tetrahedral $[GaO_4]$ in **ε-$GaAl_{12}$** was less distorted than $[AlO_4]$ in **ε-Al_{13}**.[63] In 1997, Parker and coworkers demonstrated that the substitution of only Ga^{3+} ions in **ε-Al_{13}** proceeded preferentially among Fe^{3+}, Zn^{2+}, Ga^{3+}, In^{3+}, Sn^{2+}, La^{3+}, and Bi^{3+} ions.[64] More recently, in 2015, Navrotsky and coworkers calculated the formation enthalpies of **ε-Al_{13}**, **ε-$GaAl_{12}$**, and **ε-$GeAl_{12}$** using solution calorimetry and found that stability increase in the order of **ε-$GeAl_{12}$** < **ε-$GaAl_{12}$** < **ε-Al_{13}**, indicating that changes in element and charge decrease stability.[65,66] Importantly, **ε-Al_{13}** and its derivatives lie closer in energy to solid-state Al oxides and hydroxides than to aqueous Al monomer ions, suggesting their role as metastable precursors of solid-state materials.

In 2003, Kwon and coworkers extended the transition metal substitution to larger **Al_{30}** clusters, resulting in W-substituted $[W_2Al_{28}O_{18}(OH)_{48}(H_2O)_{24}]^{12+}$ (**W_2Al_{28}**) clusters (Fig. 3c).[67] **W_2Al_{28}** was produced by reacting **Al_{30}** with $[H_2W_{12}O_{40}]^{6-}$ as the W source. In **W_2Al_{28}**, two of the four $[AlO_4]$ units between monomeric **Al_{13}** of dimeric **Al_{30}** were replaced with $[WO_4]$. In

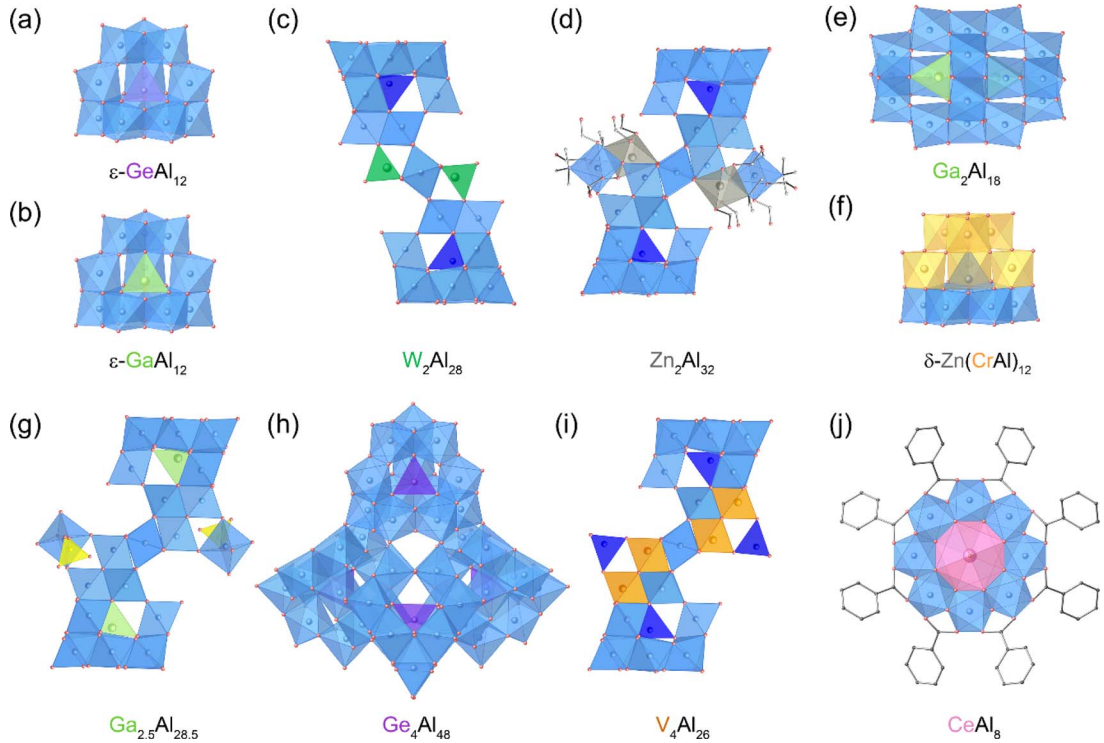

Fig. 3 Molecular structure of (a) $[\varepsilon\text{-}GeO_4Al_{12}(OH)_{24}(H_2O)_{12}]^{8+}$ (**ε-GeAl$_{12}$**), (b) $[\varepsilon\text{-}GaO_4Al_{12}(OH)_{24}(H_2O)_{12}]^{7+}$ (**ε-GaAl$_{12}$**), (c) $[W_2Al_{28}O_{18}(OH)_{48}(H_2O)_{24}]^{12+}$ (**W$_2$Al$_{28}$**), (d) $[(Zn(NTA)H_2O)_2(Al(NTA)(OH)_2)_2(Al_{30}O_8(OH)_{60}(H_2O)_{20}]^{18+}$ (**Zn$_2$Al$_{32}$**), (e) $[Ga_2Al_{18}O_8(OH)_{36}(H_2O)_{12}]^{8+}$ (**Ga$_2$Al$_{18}$**), (f) $[\delta\text{-}ZnO_4Al_{5.1}Cr_{6.9}(OH)_{24}(H_2O)_{12}]^{6+}$ (**δ-Zn(CrAl)$_{12}$**), (g) $[Ga_2O_8Al_{28.5}Ga_{0.5}(OH)_{58}(H_2O)_{27}(SO_4)_2]^{15+}$ (**Ga$_{2.5}$Al$_{28.5}$**), (h) $[Ge_4O_{16}Al_{48}(OH)_{108}(H_2O)_{24}]^{20+}$ (**Ge$_4$Al$_{48}$**), (i) $[V_4Al_{28}O_{20}(OH)_{52}(H_2O)_{22}]^{12+}$ (**V$_4$Al$_{28}$**), and (j) $[Al_8Ce(\mu_2\text{-}OH)_8(\mu_3\text{-}OH)_8(benzoate)_8(H_2O)_2]^{3+}$ (**CeAl$_8$**). $[AlO_6]$, $[AlO_4]$, and $[SO_4]$ are shown by the light blue, dark blue, and yellow polyhedrons, respectively.

2013, Forbes and coworkers reported Zn-substituted **Zn$_2$Al$_{32}$** cluster with the formula of $[(Zn(NTA)H_2O)_2(Al(NTA)(OH)_2)_2(Al_{30}O_8(OH)_{60}(H_2O)_{20}]^{18+}$ (NTA = nitrilotriacetic acid, Fig. 3d).[68] **Zn$_2$Al$_{32}$** contains **Al$_{32}$** clusters with two additional $[ZnO_6]$ units chelated by NTA, which are connected to the central part of **Al$_{32}$**.

Metal-substitution in Al oxo-hydroxide clusters can lead to the discovery of unprecedented structure motifs. In 2015, Mason, Forbes, and coworkers reported cationic variations on the Wells–Dawson topology, $[Ga_2Al_{18}O_8(OH)_{36}(H_2O)_{12}]^{8+}$ (**Ga$_2$Al$_{18}$**, Fig. 3e), by hydrolyzing a mixed aqueous solution containing Al^{3+} and Ga^{3+} ions using a low-temperature hydrothermal method.[69] **Ga$_2$Al$_{18}$** cluster has a metal ratio similar to the typical Wells–Dawson structure $[X_2M_{18}O_{62}]^{n-}$. However, the structural topology of **Ga$_2$Al$_{18}$** differs from that of anionic Wells–Dawson-type POMs. **Ga$_2$Al$_{18}$** clusters are composed of a complete ε-Keggin cluster unit (**ε-GaAl$_{12}$**) linked to a lacunary fragment, which includes a hexametric unit consisting of one $[Al_3(\mu_2\text{-}OH)_6(H_2O)_3]$ trimer and three additional edge-sharing Al(III) octahedra bonded on the exterior edges. In contrast, Wells–Dawson-type POMs are composed of two α-Keggin fragments.

Substitution of multiple types of transition metal ions into Al oxo-hydroxide clusters has been achieved. In 2016, Nyman and coworkers reported the incorporation of Zn^{2+} and Cr^{3+} ions into **δ-Al$_{13}$** analogues, $[\delta\text{-}ZnO_4Al_{5.1}Cr_{6.9}(OH)_{24}(H_2O)_{12}]^{6+}$ (**δ-Zn(CrAl)$_{12}$**, Fig. 3f), where the rotated trimer units are capped with $[Zn(H_2O)_3]^{2+}$.[70] **δ-Zn(CrAl)$_{12}$** was obtained by evaporating an aqueous solution with high concentrations of Al, Cr, and Zn species. X-ray structure and derived bond valence sums (BVSs) suggest that Zn^{2+} ions are located in the tetrahedral center of **δ-Zn(CrAl)$_{12}$**, while Al^{3+}/Cr^{3+} ions occupy the octahedral sites with site disordering. The Al/Cr ratios are higher near the rotated trimer units. In 2021, Mason and coworkers demonstrated the substitution of Cr^{3+} ions in **δ-Al$_{13}$** to synthesize $[AlO_4Al_{9.6}Cr_{2.4}(OH)_{24}(H_2O)_{12}]^{7+}$ (**δ-Al$_{10.6}$Cr$_{2.4}$**).[71] DFT study suggested that Cr^{3+} substitution occurs exclusively at the octahedral positions.

Formation of larger clusters using metal-substituted Al-based clusters as building units has been demonstrated. In 2020, Forbes and coworkers synthesized $[\delta\text{-}GaO_4Al_{12}(OH)_{24}(H_2O)_{12}]^{7+}$ (**δ-GaAl$_{12}$**), where the central tetrahedral site was substituted with $[GaO_4]$, by thermal aging of **ε-GaAl$_{12}$**.[72] The reaction of **δ-GaAl$_{12}$** with an aqueous K_2SO_4 solution forms a larger cluster of $[Ga_2O_8Al_{28.5}Ga_{0.5}(OH)_{58}(H_2O)_{27}(SO_4)_2]^{15+}$ (**Ga$_{2.5}$Al$_{28.5}$**, Fig. 3g): the core cluster **Ga$_{2.5}$Al$_{27.5}$**, which is isostructural with **Al$_{30}$**, is connected with an additional anionic unit ($[Al(OH)_2(H_2O)_3(SO_4)]^-$). X-ray structural analysis indicates that the Ga occupancy in **Ga$_{2.5}$Al$_{28.5}$** is the highest at the tetrahedral center sites (99.0%) and the second highest at the octahedral sites that bridge the nanocluster halves in the beltway region (26.9%). In 2021, the same group synthesized a giant (*ca.* 2.4 nm) Ge-substituted cluster, $[Ge_4O_{16}Al_{48}(OH)_{108}(H_2O)_{24}]^{20+}$ (**Ge$_4$Al$_{48}$**, Fig. 3h), by thermally aging **ε-GeAl$_{12}$**.[73] In **Ge$_4$Al$_{48}$**, four

ε-GeAl$_{12}$ units are linked *via* twelve μ_2-OH bridging groups in a T_d arrangement. DFT calculations indicated that Ge substitution at the central tetrahedral site of **ε-GeAl$_{12}$** is essential for forming the tetrameric **Ge$_4$Al$_{48}$**, as this substitution facilitates the deprotonation of η_1-H_2O to form symmetric μ_2-OH bridges, which can then link together to form the tetrameric **Ge$_4$Al$_{48}$**. In 2022, we reported a V-substituted $[V_4Al_{28}O_{20}(OH)_{52}(H_2O)_{22}]^{12+}$ (**V$_4$Al$_{28}$**, Fig. 3i) cluster by reacting **δ-Al$_{13}$** with $[PW_9V_3O_{40}]^{6-}$ as a V^{5+} source using a low-temperature hydrothermal method.[74] **V$_4$Al$_{28}$** contains two **δ-VAl$_{12}$** units, which is similar to **δ-Al$_{13}$**, but with one $[AlO_6]$ unit of the 60°-rotated $[Al_3O_{13}]$ trimer replaced with a $[VO_6]$ unit. The **δ-VAl$_{12}$** units are bridged by two $[AlO_6]$ and two $[VO_6]$ through corner-sharing and edge-sharing, respectively, to form **V$_4$Al$_{26}$**, which is isostructural with **Al$_{30}$**. The two additional $[AlO_4]$ units each link two $[VO_6]$ of **V$_4$Al$_{26}$** through corner-sharing, resulting in **V$_4$Al$_{28}$** with C_{2h} symmetry.

The incorporation of metal ions into Al oxo-hydroxide clusters has been extended to rare earth ions.[75] In 2023, Fang and coworkers heated a mixture of Al^{3+} ions and lanthanide (Ln) ions with benzoic acid, pyridine, and tetraethylammonium chloride in MeCN at 80 °C, resulting in the formation of $[Al_8Ln(\mu_2\text{-}OH)_8(\mu_3\text{-}OH)_8(benzoate)_8(H_2O)_2]^{3+}$ (Ln = La^{3+}, Ce^{3+}, Pr^{3+}, and Nd^{3+}), **LnAl$_8$**, Fig. 3j). In **LnAl$_8$**, Ln ions are situated at the center of the Al_8 ring clusters.

3. Assembly of Al oxo-hydroxide clusters for functional applications

3.1 Adsorption and coagulation

Adsorption and coagulation are fundamental techniques for the removal of targeted substances, and have practical applications in diverse fields, including separation science and environmental chemistry. In particular, adsorption involves the uptake of substances by a solid adsorbent through chemical and/or physical interactions between the substances and the surface of the adsorbent. Coagulation, on the other hand, is a process that occurs during precipitation, wherein additional substances are incorporated into the particles as they form from a solution. In particular, aluminum hydroxides are widely used as adsorbents and in coagulation processes due to the amphoteric character and multiple types of interactions. Adsorption and coagulation processes involve various interactions (Coulombic and van der Waals interactions), bonding mechanisms (hydrogen and covalent bonds), and surface ligand exchanges (OH/X, where X represents halogen ions, *etc.*). These interactions are facilitated by the cationic nature of aluminum and the presence of labile hydroxide and aqua ligands. Therefore, a promising approach to grant adsorptive properties to Al oxo-hydroxide cluster-based materials is to increase the surface area and construct a porous structure. A landmark work in this field was reported by Kwon and coworkers in 2000, where they demonstrated that an ionic crystal of **ε-Al$_{13}$** and Anderson-type POM $[Al(OH)_6Mo_6O_{18}]^{3-}$ (**AlMo$_6$**), $[\varepsilon\text{-}AlO_4Al_{12}(OH)_{24}(H_2O)_{12}][Al(OH)_6Mo_6O_{18}]_2(OH)\cdot 29.5H_2O$ (**ε-Al$_{13}$-AlMo$_6$**, Fig. 4a),[81] possesses porous 2D channels with dimensions estimated to be 3.1 × 5.9 Å^2 for the smallest and 6.2 × 3.9 Å^2 for the widest cross-sectional areas, showing reversible water adsorption properties. Later, they constructed various porous ionic crystals by changing the combination Al oxo-hydroxide clusters and POMs.[67,82,83]

The formation of supramolecular cage crystals is a promising method to build porous structures. In 2021, Fang, Zhang, and coworkers assembled an eight-membered Al_8 ring, $[Al_8(4\text{-chloropyrazolate})_8(OH)_8(benzoate)_8]$, through π– π interactions between adjacent Al_8 rings.[76] As a result, a $(Al_8)_6$ nanocage (**AlOC-27-NC**), in which six Al_8 rings occupying the six faces of the cube, was constructed. **AlOC-27-NC** demonstrates a high iodine (I_2) vapor saturation uptake capacity of 503 mg g^{-1} at 80 °C, attributed to strong I···π interactions between molecular I_2 and the phenyl-based linkers of **AlOC-27-NC** (Fig. 4b). In 2021, the same group demonstrated coordination-driven self-assembly of Al_8 ring, incorporating isonicotinic (INA) linkers, with Cu^{2+} ions to construct $[Al_{12}Cu_5(OH)_6(INA)_{18}(OPr^n)_{12}(H_2O)_2]\cdot 5NO_3^-$ (**AlOC-83**).[84] **AlOC-83** exhibits a remarkable capacity for the rapid removal of I_2 from cyclohexane solutions, with a considerable loading capacity of 555 mg g^{-1}. In 2022, the same group synthesized an Al_{24} cluster-based cage structure with benzoate ligands, $[Al_{24}(benzoate)_{12}(EtO)_{24}(OH)_{32}]\cdot(NO_3)_4\cdot(HOEt)_2\cdot(H_2O)_2$ (**AlMC-1**).[56] The Brunauer–Emmett–Teller (BET) specific surface area of **AlMC-1** was estimated to be 233 m^2 g^{-1} by the N_2 sorption isotherm at 77 K. **AlMC-1** enables rapid iodine capture from low-concentration aqueous I_2/KI solutions (down to 4 ppm) with the aid of cooperative I···π, C–H···I, and OH···I interaction within the pores. The adsorption capacity using a 100 000 ppm I_2/KI solution was estimated as 820 mg g^{-1}.

In 2023, Maurin, Senker, Inge, Stock, and coworkers reported a series of Al_{24} cluster-based porous salts with acetate (CH_3COO^-) ligands, $[Al_{24}(OH)_{56}(CH_3COO)_{12}]X_4$ (**CAU-55-X**, X = Cl^-, Br^-, I^-, HSO_4^-, Fig. 4c).[85] The N_2 sorption isotherm of **CAU-55-Cl** at 77 K suggests a high BET specific surface area of 490 m^2 g^{-1}. Because of the cationic nature of the Al_{24} clusters, in particular, **CAU-55-HSO$_4$** effectively adsorbs the anionic dye Alizarin Red S (ARS), with a high adsorption capacity of 239 mg g^{-1}. In 2022, Li and coworkers employed the Al_{24} cage as a building unit for metal–organic framework (MOF).[77] Specifically, the Al_{24} cage, capped with 4-pyrazolecarboxylate ($HPyC^-$), was coordinated with Cu^I ions, resulting in the formation of $[Al_{24}(OCH_3)_{24}(OH)_{32}(HPyC)_6][(HPyC)_2Cu_{0.7}\square_{0.3}]_3\cdot(CH_3COO)\cdot Cl_{5.1}$ (□ = Cu^I vacancy, **FDM-91**). Furthermore, the $[Cu(HPyC)_2]^-$ complex linker in **FDM-91** is substituted with 1,1′-biphenyl-4,4′-dicarboxylate (BPDC), yielding $[Al_{24}(OCH_3)_{12}(OH)_{44}(HPyC)_6(BPDC)_3]\cdot(CH_3COO)\cdot Cl_3$ (**FDM-92**, Fig. 4d), which exhibits exceptional water adsorption capacity (0.53 g g^{-1} at 298 K) among benchmark MOFs.

Not only crystalline materials but also amorphous materials can be utilized as adsorbents. In 2018, we synthesized amorphous high-surface-area aluminium hydroxide-bicarbonates (**Al$_{13}$-HCO$_3$**) by reacting **ε-Al$_{13}$** with sodium bicarbonate.[86] In 2020, **Al$_{13}$-HCO$_3$** was applied as adsorbent to remove the anionic dye methyl orange (MO) from water, achieving over 90% MO removal within 10 min (Fig. 4e).[78] This high removal efficiency is attributed to the electrostatic interaction between the anionic

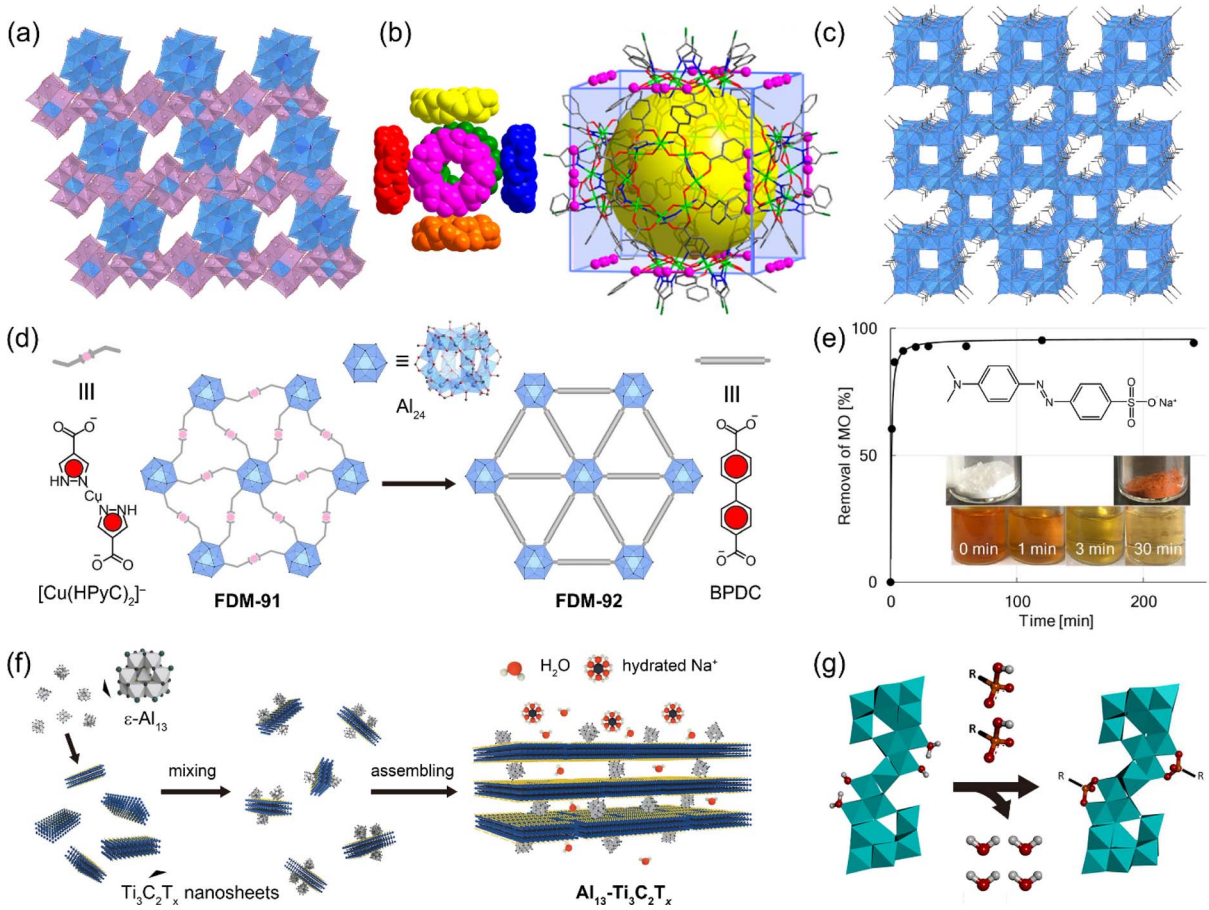

Fig. 4 (a) Crystal structure of $[\varepsilon\text{-}AlO_4Al_{12}(OH)_{24}(H_2O)_{12}][Al(OH)_6Mo_6O_{18}]_2(OH)\cdot 29.5H_2O$ (**ε-Al$_{13}$-AlMo$_6$**). [AlO_6], [AlO_4], and [MoO_6] are shown by the light blue, dark blue, and light magenta polyhedrons, respectively. Water was omitted for clarity. (b) Space-filling representation of the cuboidal $(Al_8)_6$ nanocage packing in **AlOC-26-NC**, along with a diagram illustrating the distribution of I_2 molecule around nanocages in **AlOC-26-NC** (this figure has been reproduced from ref. 76 with permission from the American Chemical Society, copyright 2021). (c) Crystal structure of $[Al_{24}(OH)_{56}(CH_3COO)_{12}]Cl_4$ (**CAU-55-Cl**), in which chloride was omitted for clarity. (d) Structural transformation from **FDM-91** to **FDM-92** by linker exchange (this figure has been reproduced from ref. 77 with permission from the Wiley-VCH GmbH, copyright 2023). (e) Time course of removal of MO from water with **Al$_{13}$-HCO$_3$**. Experimental data (closed circles) were fitted with the pseudo-second-order model (black line, this figure has been reproduced from ref. 78 with permission from the American Chemical Society, copyright 2020). (f) Schematic illustration of the fabrication of 2D lamellar **Al$_{13}$-Ti$_3$C$_2$T$_x$** (this figure has been reproduced from ref. 79 with permission from the American Chemical Society, copyright 2020). (g) A graphical depiction of the adsorption reaction of *t*-butylphosphonate (TBP) to **Al$_{30}$** to form $[(TBP)_2Al_2(\mu_4\text{-}O_8)(Al_{28}(\mu_2\text{-}OH)_{56}(H_2O)_{22})]^{14+}$ (this figure has been reproduced from ref. 80 with permission from the American Chemical Society, copyright 2015).

MO and the coordinatively unsaturated cationic **Al$_{13}$** species, which form under slightly basic synthetic conditions.

Hybridization of Al oxo-hydroxide clusters is also effective in forming porous structures. In 2020, Wang and coworkers fabricated 2D lamellar membranes using **ε-Al$_{13}$** as pillars in 2D $Ti_3C_2T_x$ nanosheets, where T_x represents surface functional groups such as –OH, –F, and =O (Fig. 4f).[79] The interlayer spacing of **Al$_{13}$-Ti$_3$C$_2$T$_x$** can be precisely modulated with angstrom-level accuracy over a wide range (2.7–11.2 Å) to achieve selective ion sieving. **Al$_{13}$-Ti$_3$C$_2$T$_x$** was applied in osmosis desalination processes, demonstrating high NaCl exclusion (99%) with a fast water flux (0.30 L m^{-2} h^{-1} bar^{-1}).

Al oxo-hydroxide clusters are also suitable as coagulants in wastewater treatment. In particular, polyaluminum chloride (PACl), obtained by the hydrolysis of aqueous $AlCl_3$ solution, is a commonly used coagulant that achieves superior removal of dissolved organic carbon (DOC) compared to alum.[87] PAC includes three Al species: monomeric Al_a, medium polymeric Al_b, and high polymeric Al_c.[88,89] It is generally believed that one of the Al_b and Al_c species corresponds to **Al$_{13}$** and **Al$_{30}$**, respectively.[90] The charge neutralization capacity of PACl with a high **Al$_{30}$** content (PAC-Al_{30}) is slightly lower than that of PACl with a high **Al$_{13}$** content (PAC-Al_{13}) at pH ≥ 6.8, whereas it is higher pH ≤ 6.5.[91] The use of Al oxo-hydroxide clusters as coagulants has been explored not only with PACls that contain a mixture of clusters of various sizes, but also with isolated single-size clusters. In 2015, Forbes, Mason, and coworkers employed **Al$_{30}$** to remove an organo-phosph(on/in)ate, *t*-butylphosphonate (TBP), from an aqueous solution.[80] TBP coordinated in the central beltway region of **Al$_{30}$** and formed a bridging bidentate configuration through ion-pair formation and ligand exchange, resulting in the formation of $[(TBP)_2Al_2(\mu_4\text{-}O_8)(Al_{28}(\mu_2\text{-}$

$OH)_{56}(H_2O)_{22})]^{14+}$ (Fig. 4g). In 2021, Shohel, Forbes, and coworkers demonstrated the removal of humic acid (HA) from Iowa river water by coprecipitating with **ε-Al$_{13}$**, **ε-GaAl$_{12}$**, or **ε-GeAl$_{12}$**.[92] The HA removal efficiency increased with decreasing pH, reaching *ca.* 85% at pH = 5 for all three clusters, due to the presence of labile protons on their surfaces, which enable the neutralization of HA.

3.2 Catalysis

Catalysts mediate various chemical reactions and play a crucial role in chemical production.[93] Al oxo-hydroxide clusters possess large numbers of hydroxyl/aqua ligands and have been applied as Brønsted acid catalysts. In 2016, we reacted **ε-Al$_{13}$** with Keggin-type POM $[\alpha\text{-}CoW_{12}O_{40}]^{6-}$ (**CoW$_{12}$**) to crystallize needle-type crystals of $[\varepsilon\text{-}Al_{13}O_4(OH)_{24}(H_2O)_{12}][\alpha\text{-}CoW_{12}O_{40}](OH)\cdot nH_2O$ (**ε-Al$_{13}$-CoW$_{12}$-*N***) possessing nanochannels with an aperture of *ca.* 6 Å × 6 Å.[94] **ε-Al$_{13}$-CoW$_{12}$-*N*** exhibited moderate catalytic activity for the acid-catalyzed pinacol rearrangement at 100 °C for 40 h in toluene (with 31% conversion and 18% yield of pinacolone, Fig. 5a). We found that adding NaCl to the synthetic solution of **ε-Al$_{13}$-CoW$_{12}$-*N*** produced plate-type crystals of **ε-Al$_{13}$-CoW$_{12}$-*P*** (Fig. 5b), which is a polymorph of **ε-Al$_{13}$-CoW$_{12}$-*N***. **ε-Al$_{13}$-CoW$_{12}$-*P*** possesses multiple hydrogen bonds between **ε-Al$_{13}$** and **CoW$_{12}$** and is structurally stable, featuring one-dimensional channels with an aperture of *ca.* 12 Å × 6 Å, which is larger than that of **ε-Al$_{13}$-CoW$_{12}$-*N*** (*ca.* 6 Å × 6 Å). We concluded that the formation of **ε-Al$_{13}$-CoW$_{12}$-*P*** is attributed to the deshielding of electrostatic interaction between **ε-Al$_{13}$** and **CoW$_{12}$** by Na^+ and Cl^-, which slows crystallization and allows the transformation into a more stable polymorph with a larger number of hydrogen bonds. The catalytic activity of **ε-Al$_{13}$-CoW$_{12}$-*P*** (with 76% conversion and 54% yield of pinacolone) is higher than that of **ε-Al$_{13}$-CoW$_{12}$-*N*** (with 31% conversion and 18% yield of pinacolone) under the same reaction conditions. These results demonstrate that controlling crystal polymorph, which lead to the expansion of channel apertures, improves catalytic activity.

Additionally, we investigated the isomeric effect of **Al$_{13}$** on catalytic activity. In 2021, we crystallized **δ-Al$_{13}$**, which is a rotational isomer of **ε-Al$_{13}$**, with **CoW$_{12}$** to construct $[\delta\text{-}Al_{13}O_4(OH)_{24}(H_2O)_{12}][\alpha\text{-}CoW_{12}O_{40}](OH)\cdot nH_2O$ (**δ-Al$_{13}$-CoW$_{12}$**, Fig. 5c)[67,96] **δ-Al$_{13}$-CoW$_{12}$** effectively catalyzed pinacol rearrangement at 100 °C and 10 h in toluene (with 100% conversion and 75% yield of pinacolone), which is superior to that of **ε-Al$_{13}$-CoW$_{12}$-*N*** under identical conditions. The enhanced catalytic activity of **δ-Al$_{13}$-CoW$_{12}$** is attributable to increased Brønsted acidity in **δ-Al$_{13}$**. The increased acidity in **δ-Al$_{13}$** can be explained by the shorter average Al–O bond distance in **δ-Al$_{13}$** compared to **ε-Al$_{13}$**, as a shorter Al–O distance weakens the O–H bond of the aqua ligand, thereby increasing Brønsted acidity.

Supramolecular cages based on Al oxo-hydroxide clusters have shown promise as heterogeneous catalysts. In 2023, Fang, Zhang, and coworkers reported an intriguing hydrogen bonding assembly from convex-concave $[Al_6Co_3(OH)_4(CAT)_3(HCAT)_9]^{5+}$ (H_2CATs = catechol ligands) into a truncatedhexahedron Archimedean $\{Al_6Co_3\}_8$ supramolecular cage, $[(Al_6Co_3(OH)_4(CAT)_3(HCAT)_9)_8\cdot nDMF\cdot 8OAc\cdot 7CAT\cdot 2HCAT\cdot 12O^iPr]^{4+}$ (n = 0–18).[97] The supramolecular cage effectively catalyzed the aldol condensation of acetone and *p*-nitrobenzaldehyde to yield β-hydroxy ketone at 60 °C and 48 h in DMSO, achieving a 75% yield.

Al oxo-hydroxide clusters can function not only as Brønsted acid catalysts but also as Lewis acid catalysts. In 2022, we crystallized $[V_4Al_{28}O_{20}(OH)_{52}(H_2O)_{22}]^{12+}$ (**V$_4$Al$_{28}$**, Fig. 3i) with $[PW_9V_3O_{40}]^{6-}$ (**PW$_9$V$_3$**) to form $[V_4Al_{28}O_{20}(OH)_{52}(H_2O)_{22}][\alpha\text{-}PW_9V_3O_{40}]_2\cdot 55H_2O$ (**V$_4$Al$_{28}$-PW$_9$V$_3$**).[74] **V$_4$Al$_{28}$** possesses exposed $[AlO_4]$ tetrahedra, which are expected to act as Lewis acid sites.

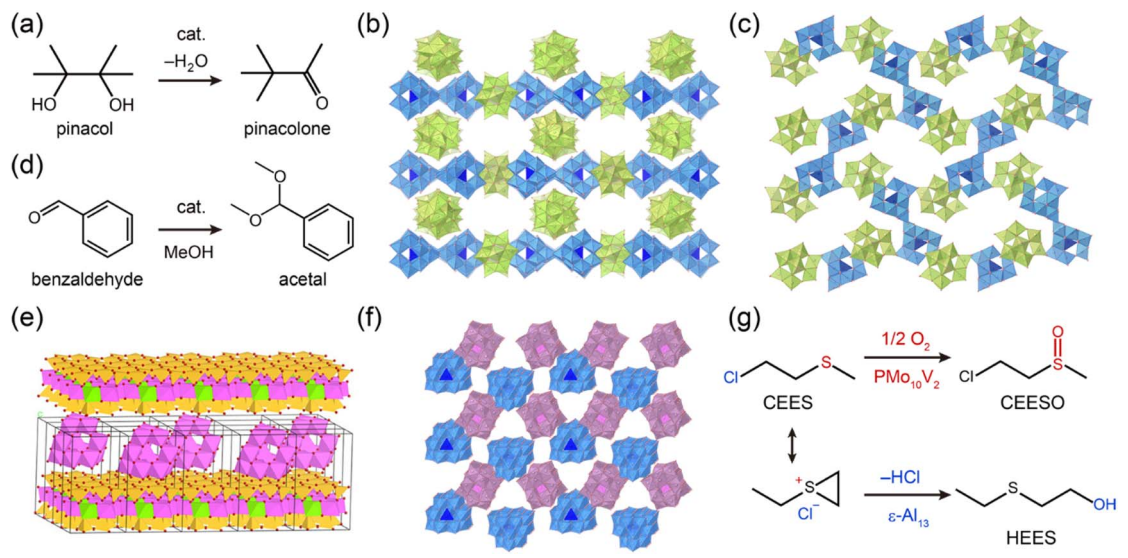

Fig. 5 (a) Acid-catalyzed pinacol rearrangement. Crystal structure of (b) $[\varepsilon\text{-}Al_{13}O_4(OH)_{24}(H_2O)_{12}][\alpha\text{-}CoW_{12}O_{40}](OH)\cdot nH_2O$ (**ε-Al$_{13}$-CoW$_{12}$-*P***) and (c) $[\delta\text{-}Al_{13}O_4(OH)_{24}(H_2O)_{12}][\alpha\text{-}CoW_{12}O_{40}](OH)\cdot nH_2O$ (**δ-Al$_{13}$-CoW$_{12}$**). $[AlO_6]$, $[AlO_4]$, and $[CoO_4]$ are shown by the light blue, dark blue, and light pink polyhedrons, respectively. (d) Acetalization of benzaldehyde with methanol. (e) Arrangement models of **ε-Al$_{13}$** in the interlayer region of montmorillonite (this figure has been reproduced from ref. 95 with permission from the American Chemical Society, copyright 2019). (f) Crystal structure of $[\varepsilon\text{-}Al_{13}O_4(OH)_{24}(H_2O)_{12}][\alpha\text{-}PMo_{10}V_2O_{40}](OH)_2\cdot 20H_2O$ (**ε-Al$_{13}$-PMo$_{10}$V$_2$**). $[AlO_6]$, $[AlO_4]$, $[PO_4]$ and $[MoO_6]$ are shown by the light blue, dark blue, dark pink and light magenta polyhedrons, respectively. (g) Proposed dual-mechanism degradation of CEES by **ε-Al$_{13}$-PMo$_{10}$V$_2$**.

The catalytic activity of $\mathbf{V_4Al_{28}\text{-}PW_9V_3}$ was investigated by acetalization of benzaldehyde with methanol to produce benzaldehyde dimethyl acetal at 70 °C after 2 h (Fig. 5d). The catalytic activity of $\mathbf{V_4Al_{28}\text{-}PW_9V_3}$ (with 53% yield) is higher than that of **δ-Al$_{13}$-CoW$_{12}$** (with 41% yield), $[\delta\text{-}Al_{13}O_4(OH)_{24}(H_2O)_{12}][PW_9V_3O_{40}](OH)\cdot 24H_2O$ (**δ-Al$_{13}$-PW$_9$V$_3$**, with 40% yield), and **ε-Al$_{13}$-CoW$_{12}$-*P*** (with 41% yield), which do not have the exposed $[AlO_4]$ sites. These observations highlight that the Lewis acid sites of $\mathbf{V_4Al_{28}\text{-}PW_9V_3}$ play a critical role in the acetalization reaction.

Transition metal substituted Al oxo-hydroxide clusters show potential also as electrocatalysts. In 2023, Liu and coworkers reported $[Co_4Al_{12}O_8(OH)_{10}(TBC[4])_4(DMF)_8Cl_2]$ (TBC[4] = *t*-butylcalix[4]arene) (**Co$_4$Al$_{12}$**) with catalytically active surface-exposed Co^{2+} sites.[98] The deposition of **Co$_4$Al$_{12}$** on carbon nanotubes (CNTs) forms **Co$_4$Al$_{12}$/CNT**. **Co$_4$Al$_{12}$/CNT** exhibits outstanding electrocatalytic performance for the oxygen evolution reaction (OER), requiring remarkably lower overpotentials in comparison to metal oxide catalysts such as IrO_2/CNTs and Co_2O_3/CNTs. Specifically, the overpotential to achieve current density of 10, 50, 100 mA cm^{-2} for **Co$_4$Al$_{12}$/CNT** are 320, 414, and 505 mV, respectively, while the corresponding overpotentials for IrO_2/CNTs are 373, 510, and 622 mV, respectively. The superior catalysis of **Co$_4$Al$_{12}$/CNT** is attributable to a binding interaction between the exposed Co sites and OH^-, which facilitates the oxidative cleavage of O–H bonds.

Cationic Al oxo-hydroxide clusters can be used to anchor catalytically active anionic species to enhance the activity of the resulting solid catalyst. In 2010, Cabello and coworkers employed $[\varepsilon\text{-}AlO_4Al_{12}(OH)_{24}(H_2O)_{12}][Al(OH)_6Mo_6O_{18}]_2(OH)\cdot 29.5H_2O$ (**ε-Al$_{13}$-AlMo$_6$**, Fig. 4a),[81] where catalytically active **AlMo$_6$** is anchored with **ε-Al$_{13}$** as an oxidation catalyst.[99] **ε-Al$_{13}$-AlMo$_6$** showed excellent catalytic performance in two aromatic sulfide oxidation reactions: the conversion of diphenylsulfide (DPS) to diphenylsulfone in the presence of H_2O_2 (with 100% conversion and selectivity 96% in MeCN at 80 °C for 70 min) and the oxidation of dibenzothiophene (DBT) to dibenzothiophenone using *t*-BuOOH (with 22.5% conversion in decane at 75 °C for 3 h). In 2019, Zhu, Xi and coworkers utilized **ε-Al$_{13}$** and **Al$_{30}$** as inorganic pillars in montmorillonite (Mt, Fig. 5e).[95,100] The intercalation of **ε-Al$_{13}$** or **Al$_{30}$** into the interlayer region of Mt increases acidity, thereby facilitating the sorption and oxidation of toluene. In 2020, Luo and coworkers hybridized Keggin-type **Al$_{13}$** with redox-active V_2O_5 nanosheets to prepare an **Al$_{13}$–V$_2$O$_5$** nanohybrid.[101] While pristine V_2O_5 nanosheets experience agglomeration due to layer stacking, the incorporation of **Al$_{13}$** into the V_2O_5 nanosheets increases the stacking space and forms porous structures. The porous **Al$_{13}$–V$_2$O$_5$** effectively catalyzed the oxidation of benzyl alcohol to benzaldehyde in acetonitrile at 100 °C, 1 atm O_2. In 2022, Zhang, Zhong, and coworkers crystalized **ε-Al$_{13}$** with photosensitive meso-tetra(4-carboxyphenyl)porphyrin ($TCPP^{4-}$) as $(TCPP)[\varepsilon\text{-}Al_{13}O_4(OH)_{24}(H_2O)_{12}]_2(OH)_{10}\cdot 18H_2O$ (**Al$_{13}$–TCPP**).[102] **Al$_{13}$–TCPP** was applied for the photocatalytic degradation of mustard gas simulant, 2-chloroethyl ethyl sulfide (CEES). The degradation rate of CEES for **Al$_{13}$–TCPP** in methanol was 96.2% after 3 h, which is higher than that of H_4TCPP (54.7%). All these results indicate that **ε-Al$_{13}$** serves as a favourable anchor for advancing catalytic reactions.

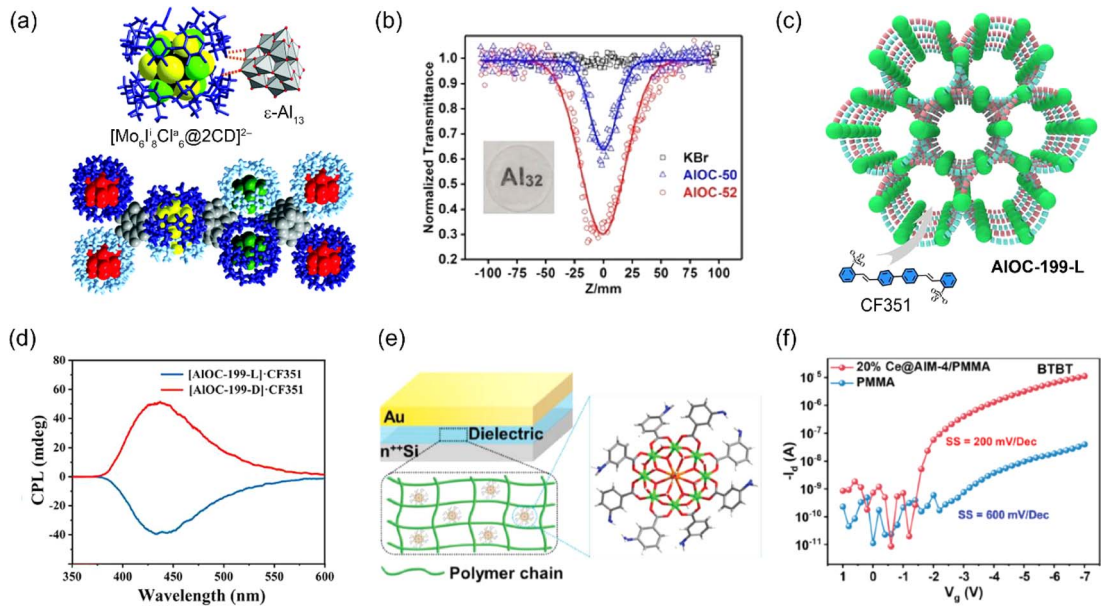

Fig. 6 (a) Interaction between $[Mo_6{}^{i}{}_8Cl_6{}^{a}@2CD]^{2-}$ and **ε-Al$_{13}$** and the packing structure of **Al$_{13}$-Mo$_6$** (this figure has been reproduced from ref. 104 with permission from the Royal Society of Chemistry, copyright 2020). (b) Open-aperture Z-scan results at 532 nm for KBr, **AlOC-50**, and **AlOC-52** (this figure has been reproduced from ref. 52 with permission from the Wiley-VCH GmbH, copyright 2021). (c) Schematic diagram illustrating the doping of fluorescent dye molecules (CF351) in chiral supramolecular structures (**AlOC-199-L**). (d) Circularly polarized luminescence (CPL)spectra of **AlOC-199-L/R**·CF351 (this figure has been reproduced from ref. 45 with permission from the American Chemical Society, copyright 2024). (e) Schematic illustration of the capacitor with **Ce@AlM-4** doped polymer dielectrics. (f) Transfer curves of the transistor with PMMA and 20% **Ce@AlM-4**/PMMA dielectrics (this figure has been reproduced from ref. 105 with permission from the Wiley-VCH GmbH, copyright 2023).

The integration of catalytically active sites from cationic Al oxo-hydroxide clusters and anionic species offers promising potential for the design of solid catalyst. In 2020, Zhang and coworkers reacted **ε-Al$_{13}$** with [α-$PMo_{10}V_2O_{40}$]$^{5-}$ (**PMo$_{10}$V$_2$**) to obtain [ε-$Al_{13}O_4(OH)_{24}(H_2O)_{12}$][α-$PMo_{10}V_2O_{40}$]$(OH)_2\cdot 20H_2O$ (**ε-Al$_{13}$-PMo$_{10}$V$_2$**, Fig. 5f).[103] **ε-Al$_{13}$-PMo$_{10}$V$_2$** acts as a dual-functional catalyst for the degradation of CEES; **ε-Al$_{13}$** hydrolyzes CEES to 2-hydroxyethyl ethyl sulfide (HEES) and **PMo$_{10}$V$_2$** oxidizes CEES to 2-chloroethyl ethyl sulfoxide (CEESO, Fig. 4g). Thus, **ε-Al$_{13}$-PMo$_{10}$V$_2$** exhibits excellent performance for the degradation of CEES with 96.4% conversion in petroleum ether solution at ambient conditions, compared to 47.2% and 21.6% conversion catalyzed by pristine **ε-Al$_{13}$** and **PMo$_{10}$V$_2$**, respectively.

3.3 Other applications

Al oxo-hydroxide clusters have been utilized as components in optical materials, where they modulate the arrangement of luminescent organic molecules and inorganic clusters. In 2020, Falaise, Cordier, and coworkers employed **ε-Al$_{13}$** as a host matrix for luminescent materials.[104] Luminescent molybdenum clusters, $[Mo_6I^i{}_8Cl_6{}^a]^{2-}$, encapsulated in γ-cyclodextrin (CD), were integrated with **ε-Al$_{13}$** to construct $\{Al_{13}\}\{[Mo_6I^i{}_8Cl_6{}^a]@2CD\}Cl_5\cdot 60H_2O$ (**Al$_{13}$-Mo$_6$**, Fig. 6a). The structural void of **Al$_{13}$-Mo$_6$** was 41%, and its quantum yield of luminescence in the red-near infrared region was 28%. In 2023, Li, Wang, and coworkers synthesized an 8-membered ring cluster, $[Al_8(OH)_8(NA)_{16}]$ (HNA = nicotinic acid), using HNA as a phosphor ligand, and demonstrated its dual luminescence properties, exhibiting fluorescence and room-temperature phosphorescence (RTP).[106] Besides, its photoluminescence was effectively regulated by the introduction of CdX_2 (X = Cl^-, Br^-, I^-) units.

Al oxo-hydroxide clusters caped with π-conjugated group can serve as third-order nonlinear optical (NLO) materials, with potential applications in photonic technologies, including optical limiting (OL) for eye protection and radiation detectors and sensors. In 2021, Fang, Zhang, and coworkers employed Al_{32} nanoflake featuring abundant π-conjugated carboxylates, specifically $[Al_{32}(benzoate)_{36}(O^iPr)_4(\mu_3\text{-}O)_{24}(\mu_4\text{-}O)_4]$ (**AlOC-50**, Fig. 1l) and $[Al_{32}(2\text{-furancarboxylate})_{36}(O^iPr)_4(\mu_3\text{-}O)_{24}(\mu_4\text{-}O)_4]\cdot 2CH_3CN$ (**AlOC-52**), as third-order NLO materials.[52] The nonlinear absorption coefficient (β) values, estimated by Z-scan curves, were 1.182×10^{-8} m W^{-1} and 4.384×10^{-8} m W for **AlOC-50** and **AlOC-52**, respectively (Fig. 6b). These values are superior to those of reported transition metal or rare-earth metal cluster-based materials. In 2022, the same groups studied the third-order NLO properties of ring-shaped Al oxo-hydroxide clusters with varying sizes and capping linkers.[54,55] As a result, they found that $[Al_{20}(phenol)_{20}(OH)_{10}(\text{-pyrenecarboxylate})_{30}]\cdot 6$phenol (**AlOC-76**) exhibits the best performance ($\beta = 7.18\times10^{-10}$ m W^{-1}) due to the strongest and diverse π–π interactions. In 2024, the same group reported the crystal-to-glass formation of a ring-shaped Al oxo-hydroxide cluster, [tetramethylammonium] ⊂ $\{Cl@[Al_8(phenol)_8(OH)_4(2\text{-naphthalenecarboxylate})_{12}]\}\cdot 2$phenol$\cdot 2$DMF (**AlOC-77-TMACl**).[107] The glassy state of **AlOC-77-TMAC** exhibited NLO properties similar to those of the crystalline state.

Al oxo-hydroxide clusters possess significant potential for use in low-cost circularly polarized luminescence (CPL) materials. In 2024, Fang and coworkers synthesized a homochiral Al oxo-hydroxide cluster, $[Al_5O_2(OH)_2(HPDA)_4(_L\text{-Val})_4]\cdot O^nPr$ (**AlOC-199-L**$\cdot O^nPr$, Fig. 1f), using pyridine-2,6-dicarboxylic acid (H_2PDA) and the chiral L-valine (L-Val) ligand.[45] **AlOC-199-L**$\cdot O^nPr$ features a hexagonal one-dimensional channel, in which the O^nPr^- ions were exchanged with an anionic fluorescent molecule, 4,4′-bis(2-sulfostyryl)biphenyl ($CF351^{2-}$), yielding **AlOC-199-L**$\cdot$CF351 (Fig. 6c). **AlOC-199-L**$\cdot$CF351 demonstrated significant CPL performance (Fig. 6d), with an absolute luminescence dissymmetry factor (g_{lum}) of up to the order of 10^{-3}, which is comparable to several noble metals.[108,109]

Recent efforts have focused on using Al oxo-hydroxide clusters as components in electronic devices, specifically field-effect transistors (FETs). In 2023, Fang, Huang, and coworkers incorporated $[Al_8Ce(\mu_2\text{-}OH)_8(\mu_3\text{-}OH)_8(BA\text{-}mNH_2)_8(H_2O)_2]\cdot 3NO_3$ (**Ce@AlM-4**), which features a central Ce(III) core connected to eight Al atoms through sixteen bridging hydroxyls and eight 3-aminobenzoate ($BA\text{-}mNH_2$) ligands, into the polymer-based dielectric layer of FETs (Fig. 6e).[105] The capacitance of polymethyl methacrylate (PMMA) films increased 2.9 times after doping with 20% **Ce@AlM-4**, resulting in a relative permittivity (k) of 9.4 at 20 Hz (Fig. 6f). Furthermore, leakage current and dielectric loss were suppressed, while the dielectric breakdown strength was enhanced. As a result, the on/off ratio of FET-**Ce@AlM-4**/PMMA (1.3×10^6) is approximately three orders of magnitude higher than that of FET-PMMA (2.7×10^3). The charge-carrier mobility (μ) of FET-**Ce@AlM-4**/PMMA reached to 2.45 $cm^2\ V^{-1}\ s^{-1}$, which is approximately 50 times higher than that of FET-PMMA.

4. Summary and outlook

In this perspective, we discussed the syntheses, molecular structures, and functional applications of Al oxo-hydroxide clusters. These clusters are formed through the hydrolysis of Al^{3+}-containing solutions, with their diversity in sizes and shapes controlled by adjusting the basicity and utilizing capping ligands. Metal substitution further enhances the compositional and structural diversity. Al oxo-hydroxide clusters have been assembled as ionic crystals, amorphous solids, and hybrid materials, demonstrating functional applications in adsorption and heterogeneous catalysis. They exhibit unique functionalities distinct from those of their anionic counterparts (*i.e.*, POMs) or bulk Al oxides/hydroxides.

We present future outlooks for Al oxo-hydroxide cluster research, focusing on (i) molecular design, (ii) synthetic methods, and (iii) functional applications. For (i) molecular design, developing Al oxo-hydroxide clusters that incorporate a wide range of lanthanide ions, such as Tb^{3+} and Dy^{3+}, holds promise for applications in single-molecule magnets (SMMs)[110] and single-molecule electrets (SMEs).[111] The utilization of these clusters to construct mechanically interlocked molecular architectures, such as catenanes and rotaxanes, presents a key

challenge.[112,113] In terms of (ii) synthetic methods, scalable and environmentally friendly techniques, such as mechanochemical synthesis, are crucial for practical applications. This approach, which involves mechanically activating solid reactants with minimal solvent, offers advantages such as reduced reaction times, increased scalability, and lower costs and environmental impact.[114,115] Moreover, it can leverage the high reactivity and structural flexibility of Al oxo-hydroxide clusters. Regarding (iii) functional applications, enhancing adsorption and catalytic properties, as well as exploring other potential applications, is particularly important. Hybridizing Al oxo-hydroxide clusters with MOFs is expected to increase the overall surface area and adsorption capacity, as observed in POM/MOF composites.[116,117] Aluminum oxides have been used to anchor metal atoms in single-atom metal catalysts,[118] and the use of Al oxo-hydroxide cluster-based solids is anticipated to fine-tune the local environment of the metal site, thereby enhancing the corresponding reaction activity. Al oxo-hydroxide clusters are characterized by a significant abundance of protons, originating from hydroxyl and aqua groups. These clusters are expected to demonstrate outstanding proton conductivity, similar to the high proton conductivity observed in cationic bismuth oxide clusters.[119] It is expected that Al oxo-hydroxide clusters, as proton donors, can be assembled with anionic proton acceptors to form polar crystals and exhibit ferroelectricity in inorganic molecular crystals.[120] We anticipate that advances in Al oxo-hydroxide clusters will contribute to both fundamental science and practical applications in the future.

Data availability

The data for this article are available from each literature cited in the reference section. The molecular and crystal structures depicted in Fig. 1–5 are drawn by us using the crystallographic information files (CIFs).

Author contributions

The manuscript was written through the contributions of all authors.

Conflicts of interest

There are no conflicts to declare.

Acknowledgements

This work was supported by grants-in-aid for scientific research (JP24H02211, 24H00463, 23K13759, 23K20034, 23H04613, 23K13759, 22H04914) from MEXT of Japan. Our collaborators inside and outside of Japan, and former and current students of Uchida group are acknowledged for their great contribution to this research.

Notes and references

1 M. Nyman, *Coord. Chem. Rev.*, 2017, **352**, 461–472.
2 D. Yang, M. Babucci, W. H. Casey and B. C. Gates, *ACS Cent. Sci.*, 2020, **6**, 1523–1533.
3 J. F. Keggin, *Nature*, 1933, **131**, 908–909.
4 M. Nyman and P. C. Burns, *Chem. Soc. Rev.*, 2012, **41**, 7354–7367.
5 Y. F. Song and R. Tsunashima, *Chem. Soc. Rev.*, 2012, **41**, 7384–7402.
6 L. Vilà-Nadal and L. Cronin, *Nat. Rev. Mater.*, 2017, **2**, 17054.
7 N. I. Gumerova and A. Rompel, *Chem. Soc. Rev.*, 2020, **49**, 7568–7601.
8 N. Ogiwara, T. Iwano, T. Ito and S. Uchida, *Coord. Chem. Rev.*, 2022, **462**, 214524.
9 W. H. Casey, *Chem. Rev.*, 2006, **106**, 1–16.
10 Z. L. Mensinger, W. Wang, D. A. Keszler and D. W. Johnson, *Chem. Soc. Rev.*, 2012, **41**, 1019–1030.
11 Y. Watanabe, K. Hyeon-Deuk, T. Yamamoto, M. Yabuuchi, O. M. Karakulina, Y. Noda, T. Kurihara, I.-Y. Chang, M. Higashi, O. Tomita, C. Tassel, D. Kato, J. Xia, T. Goto, C. M. Brown, Y. Shimoyama, N. Ogiwara, J. Hadermann, A. M. Abakumov, S. Uchida, R. Abe and H. Kageyama, *Sci. Adv.*, 2022, **8**, eabm5379.
12 K. H. Whitmire and K. Wall, *Coord. Chem. Rev.*, 2023, **488**, 215072.
13 W. H. Fang, Y. L. Xie, S. T. Wang, Y. J. Liu and J. Zhang, *Acc. Chem. Res.*, 2024, **57**, 1458–1466.
14 L. M. Cui, W. H. Fang and J. Zhang, *Chin. Chem. Lett.*, 2024, 110386, DOI: **10.1016/j.cclet.2024.110386**.
15 Y. Zhang, F. de Azambuja and T. N. Parac-Vogt, *Coord. Chem. Rev.*, 2021, **438**, 213886.
16 D. Van den Eynden, R. Pokratath and J. De Roo, *Chem. Rev.*, 2022, **122**, 10538–10572.
17 O. Sadeghi, L. N. Zakharov and M. Nyman, *Science*, 2015, **347**, 1359–1362.
18 N. P. Martin, C. Volkringer, N. Henry, X. Trivelli, G. Stoclet, A. Ikeda-Ohno and T. Loiseau, *Chem. Sci.*, 2018, **9**, 5021–5032.
19 H. G. Dill, *Earth-Sci. Rev.*, 2001, **53**, 35–93.
20 N. D. Priest, *J. Environ. Monit.*, 2004, **6**, 375–403.
21 H. Pines and W. O. Haag, *J. Am. Chem. Soc.*, 1960, **82**, 2471–2483.
22 H. Kathyayini, I. Willems, A. Fonseca, J. B. Nagy and N. Nagaraju, *Catal. Commun.*, 2006, **7**, 140–147.
23 B. N. S. Al-dhawi, S. R. M. Kutty, L. Baloo, A. M. Alawag, N. M. Y. Almahbashi, G. M. A. Naji, Y. A. A. Alsaeedi, F. A. H. Al-Towayti and A. H. Jagaba, *Case Stud. Chem. Environ. Eng.*, 2023, **7**, 100350.
24 D. Hunter and D. S. Ross, *Science*, 1991, **251**, 1056–1058.
25 R. W. Gensemer and R. C. Playle, *Crit. Rev. Environ. Sci. Technol.*, 1999, **29**, 315–450.
26 G. Furrer, B. L. Phillips, K.-U. Ulrich, R. Pöthig and W. H. Casey, *Science*, 2002, **297**, 2245–2247.
27 Y. Sakhawoth, J. Dupire, F. Leonforte, M. Chardon, F. Monti, P. Tabeling, B. Cabane, R. Botet and J. B. Galey, *Sci. Rep.*, 2021, **11**, 6376.

28 L. Liu, S. Lu, G. An, B. Yang, X. Zhao, D. Wu, H. He and D. Wang, *Coord. Chem. Rev.*, 2022, **473**, 214807.
29 C. K. Perkins, R. H. Mansergh, J. C. Ramos, C. E. Nanayakkara, D.-H. Park, S. Goberna-Ferrón, L. B. Fullmer, J. T. Arens, M. T. Gutierrez-Higgins, Y. R. Jones, J. I. Lopez, T. M. Rowe, D. M. Whitehurst, M. Nyman, Y. J. Chabal and D. A. Keszler, *Opt. Mater. Express*, 2017, **7**, 273–280.
30 G. Johansson, G. Lundgren, L. G. Sillén and R. Söderquist, *Acta Chem. Scand.*, 1960, **14**, 769–771.
31 G. Johansson, *Acta Chem. Scand.*, 1960, **14**, 771–773.
32 G. Fu, L. F. Nazar and A. D. Bain, *Chem. Mater.*, 1991, **3**, 602–610.
33 J. Rowsell and L. F. Nazar, *J. Am. Chem. Soc.*, 2000, **122**, 3777–3778.
34 S. E. Smart, J. Vaughn, I. Pappas and L. Pan, *Chem. Commun.*, 2013, **49**, 11352–11354.
35 A. F. Oliveri, C. A. Colla, C. K. Perkins, N. Akhavantabib, J. R. Callahan, C. D. Pilgrim, S. E. Smart, P. H. Cheong, L. Pan and W. H. Casey, *Chem. Eur. J.*, 2016, **22**, 18682–18685.
36 S. L. Heath, P. A. Jordan, I. D. Johnson, G. R. Moore, A. K. Powell and M. Helliwell, *J. Inorg. Biochem.*, 1995, **59**, 785–794.
37 W. Seichter, H.-J. Mögel, P. Brand and D. Salah, *Eur. J. Inorg. Chem.*, 1998, **1998**, 795–797.
38 J. T. Gatlin, Z. L. Mensinger, L. N. Zakharov, D. MacInnes and D. W. Johnson, *Inorg. Chem.*, 2008, **47**, 1267–1269.
39 W. Wang, K. M. Wentz, S. E. Hayes, D. W. Johnson and D. A. Keszler, *Inorg. Chem.*, 2011, **50**, 4683–4685.
40 W. Wang, W. Liu, I. Y. Chang, L. A. Wills, L. N. Zakharov, S. W. Boettcher, P. H. Cheong, C. Fang and D. A. Keszler, *Proc. Natl. Acad. Sci. U. S. A.*, 2013, **110**, 18397–18401.
41 B. L. Fulton, C. K. Perkins, R. H. Mansergh, M. A. Jenkins, V. Goulioukk, M. N. Jackson, J. C. Ramos, N. M. Rogovoy, M. T. Gutierrez-Higgins, S. W. Boettcher, J. F. Conley, D. A. Keszler, J. E. Hutchison and D. W. Johnson, *Chem. Mater.*, 2017, **29**, 7760–7765.
42 W. H. Casey, M. M. Olmstead and B. L. Phillips, *Inorg. Chem.*, 2005, **44**, 4888–4890.
43 K. S. Lokare, N. Frank, B. Braun-Cula, I. Goikoetxea, J. Sauer and C. Limberg, *Angew. Chem., Int. Ed.*, 2016, **55**, 12325–12329.
44 C. K. Perkins, E. S. Eitrheim, B. L. Fulton, L. B. Fullmer, C. A. Colla, D. H. Park, A. F. Oliveri, J. E. Hutchison, M. Nyman, W. H. Casey, T. Z. Forbes, D. W. Johnson and D. A. Keszler, *Angew. Chem., Int. Ed.*, 2017, **56**, 10161–10164.
45 R.-Q. Chen, S.-T. Wang, Y.-J. Liu, J. Zhang and W.-H. Fang, *J. Am. Chem. Soc.*, 2024, **146**, 7524–7532.
46 Z. Sun, H. Wang, H. Feng, Y. Zhang and S. Du, *Inorg. Chem.*, 2011, **50**, 9238–9242.
47 W. Schmitt, E. Baissa, A. Mandel, C. E. Anson and A. K. Powell, *Angew. Chem., Int. Ed.*, 2001, **40**, 3577–3581.
48 S. Abeysinghe, D. K. Unruh and T. Z. Forbes, *Cryst. Growth Des.*, 2012, **12**, 2044–2051.
49 L. Allouche, C. Gérardin, T. Loiseau, G. Férey and F. Taulelle, *Angew. Chem., Int. Ed.*, 2000, **39**, 511–514.
50 W. Yang, Z. Qian, B. Lu, J. Zhang and S. Bi, *Geochim. Cosmochim. Acta*, 2010, **74**, 1220–1229.
51 Z. Sun, H. Wang, H. Tong and S. Sun, *Inorg. Chem.*, 2011, **50**, 559–564.
52 Y. J. Liu, Q. H. Li, D. J. Li, X. Z. Zhang, W. H. Fang and J. Zhang, *Angew. Chem., Int. Ed.*, 2021, **60**, 4849–4854.
53 L. Geng, C. H. Liu, S. T. Wang, W. H. Fang and J. Zhang, *Angew. Chem., Int. Ed.*, 2020, **59**, 16735–16740.
54 Y. Li, C. Zheng, S. T. Wang, Y. J. Liu, W. H. Fang and J. Zhang, *Angew. Chem., Int. Ed.*, 2022, **61**, e202116563.
55 S. T. Wang, Y. J. Liu, C. C. Feng, W. H. Fang and J. Zhang, *Aggregate*, 2022, **4**, e264.
56 Y. J. Liu, Y. F. Sun, S. H. Shen, S. T. Wang, Z. H. Liu, W. H. Fang, D. S. Wright and J. Zhang, *Nat. Commun.*, 2022, **13**, 6632.
57 I. Ganesh, *Int. Mater. Rev.*, 2013, **58**, 63–112.
58 K. Drdlikova, R. Klement, D. Drdlik, D. Galusek and K. Maca, *J. Eur. Ceram. Soc.*, 2020, **40**, 2573–2580.
59 S. Schönherr and H. Görz, *Z. Anorg. Allg. Chem.*, 1983, **503**, 37–42.
60 A. P. Lee, B. L. Phillips, M. M. Olmstead and W. H. Casey, *Inorg. Chem.*, 2001, **40**, 4485–4487.
61 B. Thomas, H. Görz and S. Schönherr, *Z. Chem.*, 1987, **27**, 183.
62 H. Görz, S. Schönherr and F. Pertlik, *Monatsh. Chem.*, 1991, **122**, 759–764.
63 S. M. Bradley, R. A. Kydd and C. A. Fyfe, *Inorg. Chem.*, 1992, **31**, 1181–1185.
64 W. O. N. Parker Jr, R. Millini and I. Kiricsi, *Inorg. Chem.*, 1997, **36**, 571–575.
65 C. R. Armstrong, W. H. Casey and A. Navrotsky, *Proc. Natl. Acad. Sci. U. S. A.*, 2011, **108**, 14775–14779.
66 D. Reusser, W. H. Casey and A. Navrotsky, *Angew. Chem., Int. Ed.*, 2015, **54**, 9253–9256.
67 J. H. Son, Y.-U. Kwon and O. H. Han, *Inorg. Chem.*, 2003, **42**, 4153–4159.
68 S. Abeysinghe, D. K. Unruh and T. Z. Forbes, *Inorg. Chem.*, 2013, **52**, 5991–5999.
69 M. Fairley, K. W. Corum, A. Johns, D. K. Unruh, M. Basile, J. de Groot, S. E. Mason and T. Z. Forbes, *Chem. Commun.*, 2015, **51**, 12467–12469.
70 W. Wang, L. B. Fullmer, N. A. G. Bandeira, S. Goberna-Ferrón, L. N. Zakharov, C. Bo, D. A. Keszler and M. Nyman, *Chem*, 2016, **1**, 887–901.
71 J. L. Bjorklund, M. Shohel, J. W. Bennett, J. A. Smith, M. E. Carolan, E. Hollar, T. Z. Forbes and S. E. Mason, *J. Chem. Phys.*, 2021, **154**, 064303.
72 M. Shohel, J. L. Bjorklund, E. A. Ovrom, S. E. Mason and T. Z. Forbes, *Inorg. Chem.*, 2020, **59**, 10461–10472.
73 M. Shohel, J. L. Bjorklund, J. A. Smith, D. V. Kravchuk, S. E. Mason and T. Z. Forbes, *Angew. Chem., Int. Ed.*, 2021, **60**, 8755–8759.
74 W. Zhou, N. Ogiwara, Z. Weng, C. Zhao, L. Yan, Y. Kikukawa and S. Uchida, *Chem. Commun.*, 2022, **58**, 12548–12551.
75 Y.-F. Sun, Y.-J. Liu, S.-T. Wang, X.-Y. Liu, C. Ma, W.-H. Fang and J. Zhang, *Sci. China Chem.*, 2023, **66**, 1384–1393.

76 S. Yao, W. H. Fang, Y. Sun, S. T. Wang and J. Zhang, *J. Am. Chem. Soc.*, 2021, **143**, 2325–2330.
77 H. Xu, Y. Wu, L. Yang, Y. Rao, J. Wang, S. Peng and Q. Li, *Angew. Chem., Int. Ed.*, 2023, **62**, e202217864.
78 Y. Kinoshita, Y. Shimoyama, Y. Masui, Y. Kawahara, K. Arai, T. Motohashi, Y. Noda and S. Uchida, *Langmuir*, 2020, **36**, 6277–6285.
79 J. Zhu, L. Wang, J. Wang, F. Wang, M. Tian, S. Zheng, N. Shao, L. Wang and M. He, *ACS Nano*, 2020, **14**, 15306–15316.
80 K. W. Corum, M. Fairley, D. K. Unruh, M. K. Payne, T. Z. Forbes and S. E. Mason, *Inorg. Chem.*, 2015, **54**, 8367–8374.
81 J.-H. Son, H. Choi and Y.-U. Kwon, *J. Am. Chem. Soc.*, 2000, **122**, 7432–7433.
82 J.-H. Son and Y.-U. Kwon, *Inorg. Chem.*, 2004, **43**, 1929–1932.
83 J.-H. Son and Y.-U. Kwon, *Inorg. Chim. Acta*, 2005, **358**, 310–314.
84 C.-H. Liu, W.-H. Fang, Y. Sun, S. Yao, S.-T. Wang, D. Lu and J. Zhang, *Angew. Chem., Int. Ed.*, 2021, **60**, 21426–21433.
85 B. Achenbach, E. S. Grape, M. Wahiduzzaman, S. K. Pappler, M. Meinhart, R. Siegel, G. Maurin, J. Senker, A. K. Inge and N. Stock, *Angew. Chem., Int. Ed.*, 2023, **62**, e202218679.
86 Y. Kinoshita, R. Osuga, J. N. Kondo, Y. Ogasawara and S. Uchida, *Chem. Lett.*, 2018, **47**, 668–670.
87 J. Q. Jiang and N. J. D. Graham, *Environ. Technol.*, 1996, **17**, 937–950.
88 R. C. Turner, *Can. J. Chem.*, 1969, **47**, 2521–2527.
89 N. Parthasarathy and J. Buffle, *Water Res.*, 1985, **19**, 25–36.
90 Z. Wu, X. Zhang, C. Zhou, J. Pang and P. Zhang, *RSC Adv.*, 2016, **6**, 108369–108374.
91 Z. Chen, B. Fan, X. Peng, Z. Zhang, J. Fan and Z. Luan, *Chemosphere*, 2006, **64**, 912–918.
92 M. Shohel, J. A. Smith, M. A. Carolan and T. Z. Forbes, *ACS EST Water*, 2021, **2**, 22–31.
93 N. Ogiwara and S. Uchida, *Chem Catal.*, 2023, **3**, 100607.
94 K. Mizuno, T. Mura and S. Uchida, *Cryst. Growth Des.*, 2016, **16**, 4968–4974.
95 K. Wen, J. Zhu, H. Chen, L. Ma, H. Liu, R. Zhu, Y. Xi and H. He, *Langmuir*, 2019, **35**, 382–390.
96 W. Zhou, N. Ogiwara, Z. Weng, N. Tamai, C. Zhao, L. K. Yan and S. Uchida, *Chem. Commun.*, 2021, **57**, 8893–8896.
97 Y. J. Liu, H. F. Su, Y. F. Sun, S. T. Wang, C. Y. Zhang, W. H. Fang and J. Zhang, *Angew. Chem., Int. Ed.*, 2023, **62**, e202309971.
98 E.-M. Han, R.-X. Meng, Y.-Q. Tian, J. Yan, K.-Y. Liu and C. Liu, *Chem. Commun.*, 2023, **59**, 11097–11100.
99 M. Muñoz, G. Romanelli, I. L. Botto, C. I. Cabello, C. Lamonier, M. Capron, P. Baranek, P. Blanchard and E. Payen, *Appl. Catal., B*, 2010, **100**, 254–263.
100 Y. Cardona, S. A. Korili and A. Gil, *Appl. Clay Sci.*, 2021, **203**, 105996.
101 S. Wang, S. Li, R. Shi, X. Zou, Z. Zhang, G. Fu, L. Li and F. Luo, *Dalton Trans.*, 2020, **49**, 2559–2569.
102 Y. Yang, J. Yin, F. Tao, Y. Zhou, L. Zhang, Y. Zhong and Y. Wang, *RSC Adv.*, 2022, **12**, 20251–20258.
103 J. Yu, Q. Gao, L. Zhang, Y. Zhou, Y. Zhong, J. Yin, Y. Zhou, F. Tao and Y. Wang, *Dalton Trans.*, 2020, **49**, 8122–8135.
104 C. Falaise, A. A. Ivanov, Y. Molard, M. Amela Cortes, M. A. Shestopalov, M. Haouas, E. Cadot and S. Cordier, *Mater. Horiz.*, 2020, **7**, 2399–2406.
105 X. Chen, Y. F. Sun, X. Wu, S. Shi, Z. Wang, J. Zhang, W. H. Fang and W. Huang, *Adv. Mater.*, 2023, **35**, e2306260.
106 W. Lv, Y. J. Ma, A. N. Wang, Y. Mu, S. W. Niu, L. Wei, W. L. Dong, X. Y. Ding, Y. B. Qiang, X. Y. Li and G. M. Wang, *Small*, 2024, **20**, e2306713.
107 S. T. Wang, W. H. Fang and J. Zhang, *Angew. Chem., Int. Ed.*, 2024, **63**, e202400161.
108 X. Q. Liang, Y. Z. Li, Z. Wang, S. S. Zhang, Y. C. Liu, Z. Z. Cao, L. Feng, Z. Y. Gao, Q. W. Xue, C. H. Tung and D. Sun, *Nat. Commun.*, 2021, **12**, 4966.
109 Y. Shichibu and K. Konishi, *ChemNanoMat*, 2022, **8**, e202200194.
110 D. N. Woodruff, R. E. Winpenny and R. A. Layfield, *Chem. Rev.*, 2013, **113**, 5110–5148.
111 C. Kato, R. Machida, R. Maruyama, R. Tsunashima, X. M. Ren, M. Kurmoo, K. Inoue and S. Nishihara, *Angew. Chem., Int. Ed.*, 2018, **57**, 13429–13432.
112 M. Cesario, C. O. Dietrich-Buchecker, J. Guilhem, C. Pascard and J. P. Sauvage, *J. Chem. Soc., Chem. Commun.*, 1985, 244–247.
113 J. F. Stoddart, *Angew. Chem., Int. Ed.*, 2017, **56**, 11094–11125.
114 P. J. Beldon, L. Fábián, R. S. Stein, A. Thirumurugan, A. K. Cheetham and T. Friščić, *Angew. Chem., Int. Ed.*, 2010, **49**, 9640–9643.
115 K. Kubota, T. Seo, K. Koide, Y. Hasegawa and H. Ito, *Nat. Commun.*, 2019, **10**, 111.
116 A. X. Yan, S. Yao, Y. G. Li, Z. M. Zhang, Y. Lu, W. L. Chen and E. B. Wang, *Chem.–Eur. J.*, 2014, **20**, 6927–6933.
117 C. A. Nagasaka, N. Ogiwara, S. Kobayashi and S. Uchida, *Small*, 2023, e2307004.
118 Z. Zhang, Y. Zhu, H. Asakura, B. Zhang, J. Zhang, M. Zhou, Y. Han, T. Tanaka, A. Wang, T. Zhang and N. Yan, *Nat. Commun.*, 2017, **8**, 16100.
119 B. Liu, D. Cheng, H. Zhu, J. Du, K. Li, H. Y. Zang, H. Tan, Y. Wang, W. Xing and Y. Li, *Chem. Sci.*, 2019, **10**, 556–563.
120 S. Horiuchi, F. Ishii, R. Kumai, Y. Okimoto, H. Tachibana, N. Nagaosa and Y. Tokura, *Nat. Mater.*, 2005, **4**, 163–166.